TITLE

Afadin-deficient retinas exhibit severe neuronal lamination defects but preserve visual functions

Akiko Ueno[abd#], Konan Sakuta[c#], Hiroki Ono[b], Haruki Tokumoto[c], Mikiya Watanabe[c], Taketo Nishimoto[c], Toru Konishi[b], Shunsuke Mizuno[c], Jun Miyoshi[e], Yoshimi Takai[f], Masao Tachibana[a], Chieko Koike[abd]

[a]Center for Systems Vision Science, Research Organization of Science and Technology, Ritsumeikan University, Kusatsu, Shiga 525-8577, Japan,
[b]College of Pharmaceutical Sciences, Ritsumeikan University, Kusatsu, Shiga 525-8577, Japan,
[c]Graduate School of Pharmacy, Ritsumeikan University, Kusatsu, Shiga 525-8577, Japan,
[d]Ritsumeikan Global Innovation Research Organization (R-GIRO), Ritsumeikan University, Kusatsu, Shiga 525-8577, Japan,
[e]Department of Molecular Biology, Osaka Medical Center for Cancer and Cardiovascular Disease, Osaka, Japan.
[f]Division of Pathogenetic Signaling, Department of Physiology and Cell Biology, Kobe University Graduate School of Medicine, Kobe, Hyogo, Japan.
# These authors contributed equally to this work.

Corresponding author

Chieko Koike, Ph.D.

koike@fc.ritsumei.ac.jp

ABSTRACT

Neural lamination is a common feature of the central nervous system (CNS), with several subcellular structures, such as adherens junctions (AJs), playing a role in this process. The retina is also heavily laminated, but it remains unclear how laminar formation impacts retinal cell morphology, synapse integrity, and overall retinal function. In this study, we demonstrate that the loss of afadin, a key component of AJs, leads to significant pathological changes. These include the disruption of outer retinal lamination and a notable decrease as well as mislocalization of photoreceptors, their outer segments, and photoreceptor synapses. Interestingly, despite these severe impairments, we recorded small local field potentials, including the a- and b-waves. We also classified ganglion cells into ON, ON-OFF, and OFF types based on their firing patterns in response to light stimuli. Additionally, we successfully characterized the receptive fields of certain retinal ganglion cells. Overall, these findings provide the first evidence that retinal circuit function can be partially preserved even when there are significant disruptions in retinal lamination and photoreceptor synapses. Our results indicate that retinas with severely altered morphology still retain some capacity to process light stimuli.

INTRODUCTION

A common feature of the central nervous system (CNS) in vertebrates is highly laminated structures, which are established by well-ordered neuronal migration (Ayala et al., 2007; Liu, 2011; Veeraval et al., 2020). Lamination defects are observed in some patients with psychiatric disorders, such as autism spectrum disorder, and these rodent models suggest that lamination may be associated with neural circuit formation and function (Miao et al., 1994; Pan et al., 2019; Romero et al., 2018; Stouffer et al., 2016). However, several studies report that orderly lamination is dispensable for the assembly of direction-selective tectal circuits as well as for several cortical circuit functions and synaptic connections (Dräger, 1981; Guy et al., 2015; Guy and Staiger, 2017; Nikolaou and Meyer, 2015). Therefore, the full extent of the association between lamination and the integrity of neural circuit function remains elusive.

Adherens junctions (AJs), known to be correlated with CNS lamination, are adhesive intercellular junctions composed of protein complexes that mediate strong cell-cell adhesion (Harris and Tepass, 2010; Masai et al., 2003; Meng and Takeichi, 2009; Park et al., 2002; Takai et al., 2008b). Cadherin-catenin complex, nectin-afadin complex, and actin cytoskeleton are the major components of AJs (Gil-Sanz et al., 2014; Harris and Tepass, 2010; Ikeda et al., 1999; Meng and Takeichi, 2009; Tachibana et al., 2000; Takai et al., 2008b, 2008a). Cell-cell adhesion of AJs is mainly mediated by the cadherin-catenin complex, whereas nectin and afadin are required for the initial establishment of AJs (Takai and Nakanishi, 2003). A recent report shows that afadin in intestinal cells is essential

for epithelial cell-cell adhesion which was previously assumed to be primarily regulated by cadherin and catenin (Mangeol et al., 2024). Following this result, the functional importance of afadin and nectin in AJs is being reconsidered (Sebbagh and Schwartz, 2024). Animals with mutations in AJ molecules exhibit cell migration defects in the developing stage, resulting in disruption of lamination, which might be associated with brain dysfunctions, such as intellectual disability (Baum and Georgiou, 2011; de Ligt et al., 2012). However, how the defects in AJs affect the CNS function also remains unclear.

The retina, one of the best-understood mammalian neural circuits in the CNS, is highly laminated and organized into three nuclear layers and two synaptic layers (Amini et al., 2017). In the retina, incoming light is converted into neural signals in photoreceptors, processed in parallel through a network of interneurons, and finally sent to the brain via the optic nerve, the bundle of retinal ganglion cell (RGC) axons (Masland, 2012). Photoreceptors, bipolar cells (BCs), and RGCs are connected sequentially, and horizontal cells and amacrine cells (ACs) modulate the information flow in the circuit (Wässle, 2004). The mechanisms underlying retinal circuit formation and function have been actively studied, but the effects of retinal lamination disruption on retinal neural circuits remain unclear (Duan et al., 2018, 2014; Gollisch and Meister, 2010; Zapp et al., 2022). In mammals, most of the major AJ molecules belong to protein families, possibly resulting in functional redundancy with no apparent lamination phenotype in a single knockout of a member of this complex. Indeed, the loss of central AJ molecules, nectin-1 and nectin-3, does not cause severe defects in retinal

lamination (Inagaki et al., 2005). To clarify the effects of AJ molecule depletion on retinal neural circuits and cell morphology while avoiding the problem of functional redundancy, we focused on afadin, which is a scaffolding protein for nectin and has no ortholog in mice. Afadin is confirmed to be expressed in the retina (Ohama et al., 2018) and also has been shown to contribute to the accumulation of β-catenin, αE-catenin, and E-cadherin to AJs (Sakakibara et al., 2018; Sato et al., 2006).

In this study, using the *afadin* conditional knockout (cKO) mouse, we revealed that the *afadin*-deficient retinas exhibit severe pathological defects, such as outer retinal lamination disruption, as well as decrease and mislocalization of photoreceptors and their synapses. In contrast to severe disruption of the outer retina, the inner plexiform layer (IPL) structure in the inner retina was relatively intact. Using the retinas isolated from the *afadin* cKO mouse, we could record local field potentials (micro electoretinograms: mERGs) and RGC firings. Based on the light-evoked firing pattern, RGCs could be classified into ON, ON-OFF, OFF, and other types as previously established. Furthermore, the receptive field (RF) could be mapped in some RGCs. Our results suggest that neural circuits in the retina with severe defects of the outer retinal lamination and photoreceptor synapses can mediate some visual information processing.

MATERIALS and METHODS

Animals

All animal experimental protocols were conducted in accordance with local guidelines and the ARVO statement on the use of animals in ophthalmic and vision research. These procedures were approved by the Institutional Safety Committee on Recombinant DNA Experiments (approval ID R4016) and Animal Experimental Committees (approval ID BKC2022-017) of Ritsumeikan University. Mice were kept in the temperature-controlled room at 25°C with a 12 h/12 h day/night cycle. Fresh water and rodent diets were always provided.

WT, *afadin* conditional heterozygous (cHet), and cKO mice on 129S6/SvEvTac background were used in this study. The *afadin flox* mice (Majima et al., 2009) and *Dkk3-Cre* mice (Sato et al., 2007; Yamamoto et al., 2020) have been described previously. Exon 2 of the *afadin* gene is flanked by loxP sites in the *afadin flox* mice, and Cre activity is detected in the retina of the *Dkk3-Cre* mice from embryonic day 10.5 (E10.5). Mice of either sex were used for all animal experiments. The stages used for individual experiments are described in figure legends.

Immunohistochemistry

Immunohistochemical analysis was performed as described previously (Hori et al., 2019; Kubo et al., 2021). In brief, isolated mice eyes or the retina used for MEA recordings were fixed with 4% PFA in PBS for 30 min at room temperature. After three-time washes, retinas were cryoprotected by 30% sucrose in PBS

overnight, embedded in an OCT compound (Sakura, Japan), frozen on dry ice, and sectioned at 20 μm of thickness. Whole-mount immunostaining was performed as previously described with some modifications (Ueno et al., 2018). The retinas were gently peeled off from the sclera, fixed with 4%PFA in PBS for 30 min at room temperature, and washed three times. Retinal sections and whole retinas were soaked in blocking buffer (5% NDS, 0.1% Triton X-100, in 1x PBS) for 1-2 h at room temperature, and incubated with primary antibodies in blocking buffer 1 or 2 overnight at 4°C. The sections were washed with PBS three times and incubated with fluorescent dye-conjugated secondary antibodies and DAPI (1:1000) for more than 2 h at room temperature or overnight at 4°C under the light-shielded condition. The specimens were observed using a laser confocal microscope (LSM900; Carl Zeiss, Germany). The antibodies and dilution ratios were as follows; anti-l-afadin (ab90809, abcam, UK, 1:100), anti-nectin1 (D146-3, MBL, Japan, 1:100), anti-nectin2 (D083-3, MBL, Japan, 1:100), anti-nectin3 (D084-3, MBL, Japan, 1:100), anti-PKCα (P5704, Sigma, USA, 1:1000, P4334, Sigma, 1:10000), anti-SCGN (AF4878, R&D systems, USA, 1:2000), anti-Arr3 (AB15282, Millipore, USA, 1:1000), anti-Calbindin (PC253L-100, Millipore, USA,1:200), anti-ChAT (AB144P, Millipore, USA, 1:50), anti-Bassoon (SAP7F407, Enzo, USA, 1:1000), anti-mGluR6 (current study, 1:3000), anti-PSD95 (#124 014, Synaptic Systems, Germany, 1:3000), anti-GluR5 (Grik1, gift from Steve H DeVries, 1:2000), anti-PKARIIβ (#610625, BD biosciences, USA, 1:500), anti-Calretinin (PC235L-100UCN, Millipore, USA, 1:5000), anti-EAAT5 (HPA049124, Sigma, USA, 1:100), anti-vGlut1 (AB5905, Millipore, USA, 1:6000), anti-HPC-1 (S0664, Sigma, USA, 1:10000), anti-active

caspase3 (AF835, R&D Systems, USA, 1:300), anti-Chx10 (Hori et al., 2019, 1:100), anti-Otx2 (AF1979, R&D systems, USA, 1:200), anti-Glutamine synthetase (GS, MAB302, Millipore, USA, 1:500), anti-Lhx2 (sc-19344, SANTA CRUZ, USA, 1:100), anti-RBPMS (GTX118619, GeneTex, USA, 1:500), anti-Tuj1 (#801201, BioLgend, USA, 1:500), anti-AP2α (3B5-c, DSHB, USA, 1:1000), anti-Rom1 (gift from Robert Moldey, 1:10), anti-Rhodopsin (STJ95452, ST John's Laboratory, UK, 1:100), anti-S-opsin (sc-14363, SANTA CRUZ, USA, 1:500), anti-M-opsin (AB5405, Sigma, USA, 1:500), anti-β-catenin (#610153, BD bioscience, USA, 1:1000), anti-N-cadherin (#610920, BD Transduction, USA, 1:500), and anti-phospho-histone H3S10 (#06-570, Millipore, USA, 1:2000) antibodies.

Counting of retinal cells and synapses

The cell number of each retinal cell type was counted around the area 500 μm away from the optic nerve using immunostained retinal sections, and we calculated the cell number per 100 μm width of retinal section. Each retinal cell type was identified as follows: rod (Otx2 signal at the nuclear periphery), cone (Arr3+, Otx2 signal in the soma), BC (Chx10+), horizontal cell (Calbindin+ and AP2α-), AC (AP2α+), RGC (RBPMS+), and Müller glial cell (Lhx2+).

It was difficult to count the number of synapses between photoreceptors and BCs in 2D images of the cKO retina because the direction of the photoreceptor synapse was aberrant. Thus, the number of synapses was counted using 3D images reconstituted from immunostained vertical sections. The image of

vertical sections was acquired with a width (x-axis) of 126.8 μm, a length (y-axis) of 126.8 μm, and a thickness (z-axis) of 12 μm. Then, the number of synapses per 1 mm^2 of retinal surface was calculated. The regions distal to the IPL were analyzed because photoreceptor synapses were not observed below the IPL. Since the synapses between the rod photoreceptor and BC in the cHet retina were highly dense, we counted them every 1.8 μm using 2D images and integrated them. We confirmed that the number of synapses was not different between 2D and 3D images.

Processing of tissues for electron microscopy

The eyeball was removed, cut in the cornea, and fixed with 2.5% glutaraldehyde in PBS for 2.5 h on ice, and with 2% osmium tetroxide for 2 h. Retinas were washed with 1x PBS, and dehydrated with a graded series of ethanol, followed by propylene oxide, and embedded in EPON 812. Seventy-nm ultrathin sections were cut by an ultramicrotome (Ultracut E; Reichert-Jung, Germany), mounted on nickel grids, and stained with 2% uranyl acetate for 4 h and with nitrate for 5 min. Retinal sections were observed by transmission electron microscope (H-7500; HITACHI Co, Japan).

Reverse transcription real-time quantitative PCR (RT-qPCR)

Total retinal RNA was isolated using Isogen II reagent (Nippon Gene, Japan) following the manufacturer's instructions, and reverse transcribed into cDNA using SuperScript II Reverse Transcriptase (Thermo Fisher Scientific, USA) with random hexamers and oligo (dT) 12-18 primers. Diluted cDNA was used as a

template for qPCR using a TB Green® Premix Ex Taq™ II (Tli RNaseH Plus) (TaKaRa, Japan) according to the manufacturer's instructions, on Thermal Cycler Dice® Real Time System II (TaKaRa, Japan). The primer sequences are listed in **Table S1**.

Western blot analysis

Retinal tissues were lysed in RIPA buffer (50 mM Tris-HCl pH7.6, 150 mM NaCl, 1mM EDTA, pH8.0, 1% Nonided-P40, 1% Sodium Deoxycholate, 0.1% SDS), cooled for 10 min on ice, and centrifuged at 14,000 rpm for 10 min at 4°C. Then, a 3x sample buffer was added to the supernatant, and it was boiled for 10 min at 95°C. Samples were separated by SDS-PAGE and transferred to PVDF membranes (Millipore, USA) using a wet transfer cell (Bio-Rad, USA). The membranes were soaked by blocking buffer (5% skim milk (W/V) and 0.1% Tween 20 in TBS) and incubated with anti-l-afadin antibody (1:1000) overnight at 4°C or horseradish peroxidase-conjugated anti-GAPDH antibody (1:5000) for 2 h at room temperature. After washing with TBS/0.1% Tween-20 four times for 10 min each, the membranes were incubated with horseradish peroxidase-conjugated anti-mouse IgG antibody for 2 h at room temperature. Signals were detected using ImmunoStar LD (Fujifilm Wako, Japan).

Antibody production

cDNA fragments encoding a C-terminal portion of mouse mGluR6 (853-871 residues) were subcloned into *pGEX4T-1* plasmid (Amersham, UK). The GST-mGluR6 fusion protein was expressed in *Escherichia coli* strain BL21 and

purified with glutathione Sepharose 4B (GE Healthcare, USA) according to the manufacturer's instructions. The anti-mGluR6 antibody was obtained by immunizing guinea pigs with the purified GST-mGluR6.

ERG recordings

Mice were dark-adapted for more than 1 h, and then anesthetized deeply by intraperitoneally injecting mixed anesthesia consisting of (in mg/kg) 0.3 medetomidine, 4 midazolam, and 5 butorphanol tartrate. We also administered 0.1% tropicamide and 0.1% phenylephrine to the eyes to dilate the pupil. ERGs were recorded via contact lens electrodes (Mayo Corporation, Japan), and data were sampled at 1,250 Hz by using the PuREC system (Mayo Corporation, Japan). Reference and ground electrodes were placed in the mouth and on the tail, respectively. Full-field stimulation was presented via an optical stimulator equipped with white LED (RMG; Mayo Corporation, Japan), and its light intensity and duration were controlled by an LED visual stimulator (LS-100; Mayo Corporation, Japan). Scotopic ERGs were recorded by applying 5-ms flash (1.0 x 10^4 cd/m^2) three times in the dark. After 10 min light adaptation (31.6 cd/m^2), photopic ERGs were recorded by superimposing 5-ms flash (1.0 x 10^4 cd/m^2) sixteen times on the adapting background. After noise reduction by a program installed in the PuREC system, ERGs were lowpass-filtered (<50 Hz) on Python3 and then analyzed.

MEA recordings

The retinal preparation was made as described previously (Takeuchi et al.,

2018). In brief, a dark-adapted (>1 h) mouse was sacrificed by cervical dislocation under a dim red light, and its eyes were enucleated. Under a stereomicroscope equipped with an infrared (IR) image converter (V6833P, Hamamatsu Photonics, Japan) and IR illumination (HVL-IRM, Sony, Japan), the retina was isolated from the eye, and the dorsal retina was placed ganglion cell layer side down onto the multielectrode array (MEA, Multichannel Systems, Germany, 60pMEA200/30iR-Ti: 60 electrodes, electrode size 30x30 μm, inter-electrode distance 200 μm) and attached to the MEA by suction using a vacuum pump (Constant Vacuum Pump, Multichannel Systems, Germany). When another type of MEA (Multi Channel Systems, Germany, 60MEA200/30iR-Ti-gr: 60 electrodes, electrode size 30×30 μm, inter-electrode distance 200 μm) was used, a piece of anodisc (13 mm, 0.2 μm, 6809-7023, Whatman, UK) and a weight with nylon fibers were placed on the retina to improve the contact with MEA. Then, the MEA chamber was constantly superfused with Ames' medium (A1372-25, United States Biological, USA) bubbled with 95% O_2/5% CO_2 at the rate of 6.0 mL/min at 32°C. After >30 min superfusion, we started recordings. Signals were amplified, sampled at 20 kHz, and stored using MEA2100-Lite-System (Multichannel Systems, Germany). In pharmacological experiment, L-(+)-2-amino-4-phosphonobutyric acid (10 μM; L-AP4, 23052-81-5, Tocris, UK) dissolved in Ames' medium was bath-applied to the retina.

Light stimulus generated by Psychtoolbox-3 on MATLAB was presented on a monitor display (P2314H, Dell, Japan), and projected through optics on the

photoreceptor layer. Flashes (24.2 or 27.3 cd/m^2, 2 s in duration, 1,600 μm in diameter) were presented seven times every 8 s. In some experiments, the retina was stimulated by 5-ms diffuse green LED light (2.5 x 10^4 photons/s/μm^2 for mERG recordings, 4.8 x 10^3 photons/s/μm^2 for rod stimulation: LED; λ_{max} = 518 nm, IF filter; 510 nm, FWHM 10 nm, #65-697, ND filter; OD 1.0 #47-207, EDMUND OPTICS, USA) or 5-ms diffuse UV LED light (3.3 x 10^4 photons/s/μm^2 for cone stimulation; LED; λ_{max} = 370 nm, KED365UH, IF filter; 360 nm, FWHM 10 nm #67-827, EDMUND OPTICS, USA) controlled by a function generator (WF1973, NF Corporation, Japan) three times every >10 s.

Spike sorting

For spike sorting, the algorithm described on Python3 was used. The data were high pass-filtered (>300 Hz), and minimum values were detected by using scipy.signal.argrelmin function. To decide whether each detected minimum value reflects the peak of spike event, we used a threshold value defined by the following formula (Quiroga et al., 2004).

$$threshold = -4 \times median\ (|x|\ /0.6745),$$

where x represents each data point*, as* our data were recorded extracellularly, the threshold polarity was reversed. The detected values (> threshold) were judged as spike events, and the waveform of spikes was obtained from the data points between -1 and +2 ms from each peak. The 1st and 2nd differences (numpy.diff) of each waveform were joined, and then principal component analysis (PCA) was carried out for feature compression to two dimensions. Then,

clustering was performed using template matching method (Zhang et al., 2004) and Uniform Manifold Approximation and Projection (UMAP). To check the accuracy of spike sorting, we performed autocorrelation analysis to confirm the presence of a refractory period (the number of spike events at ± 1 ms bin was less than 1% of total spike events).

Classification of RGCs based on PSTH

Using the MEA system, we recorded firing responses of RGCs to light stimulation (0.24 or 0.27 cd/m^2 in intensity, 2 s in duration) presented 7 times from the monitor and calculated the peristimulus time histograms (PSTHs) with 20-ms bin. The PSTH was smoothed by a Gaussian filter (kernel size: 3 bins, σ = 1). The light-evoked response was defined when the firing rate of the PSTH exceeded the threshold (increment >+4 SDs, decrement <-2 SDs) determined by the spontaneous firing rate for 2 s before light stimulation. RGCs were classified into “ON” (increment within 2 s after light onset), “ON-OFF” (increment within 2 s after light onset and offset), “ON-OFF inhibition” (decrement within 2 s after light onset and offset), “OFF” (decrement within 2 s after light onset and/or increment within 2 s after light offset), and “None” (no clear change in firing rate) types.

To determine the type of photoreceptor inputs, a 2-s flash of green LED (λ_{max} = 510 nm, 4.8x10^3 photons/s/µm^2) and 2-s flash of UV LED (λ_{max} = 360 nm, 3.3x10^4 photons/s/µm^2) were applied seven times at 8-s interval serially. We classified RGCs into “Rod (+)” (responded to green LED), “Cone (+)-Rod (+)”

(responded to both green and UV LEDs), “Cone (+)” (responded to UV LED), and “None” responsive types.

Receptive Field

The reverse correlation method was used to detect the receptive field (RF). Pseudorandom checkerboard patterns (32×32 pixels; black/white = 1; pixel size 50×50 μm) were applied to the retina at 60 Hz. The checkerboard images that preceded each spike event (20 frames) were averaged (spike-triggered average: STA). The intensity of each pixel was +1 or -1, and thus the area with pixels that exceeded +5 SDs of the noise intensity (~0.5: the SD calculated from the frame at t = 0) were judged to be an RF, and the pixel with maximal intensity was defined as the RF center. An ellipse was fitted to the area, and its long and short axes, as well as the area, were calculated. To estimate the temporal profile of RF, the mean intensity of 5×5 pixels in the RF central region was obtained from a series of averaged frames. The temporal profile of RF was normalized, assuming that the mean of the frame at t = 0 was 0. The normalized temporal profiles were compressed to two dimensions by using UMAP, and then k-means clustering was performed.

Statistical Analysis

In Figures 3E, 3F, S3C, S3F, S3G, S3H, 4F, and 8B, the Student’s t-test was used. In Figures 5C- F and 7D, the Mann-Whitney U test was used. In Figure 6A, the Kolmogorov-Smirnov test was used. Error bars denote standard error. The following asterisks in Figures indicate *p* values: * <0.05, ** <0.01, *** <0.001.

RESULTS

Afadin is localized to adherens junctions, synaptic regions, and the surface of bipolar cells in the retina

To elucidate afadin localization in mature retina (1-month-old: 1M), we immunostained retinal sections with anti-afadin antibody. Afadin signals were observed in the outer segment (OS), outer limiting membrane (OLM), outer plexiform layer (OPL), inner nuclear layer (INL), and inner plexiform layer (IPL) (Figure 1A *Top*). These signals were not observed in retinal sections immunostained using anti-afadin antibody pre-absorbed with the antigen peptide (Figure 1A *Bottom*), suggesting that the signals are specific to afadin. To explore whether afadin is co-localized with nectins in the retina, we analyzed afadin and nectin localization in the retina by immunostaining using antibodies against afadin and nectins1-3. Afadin signals were aligned and overlapped with all three nectin signals in the OLM (Figures 1B, C, S1A), consistent with the previous finding that AJs are formed in the OLM in the retina (Willbold and Layer, 1998). Nectin-1, unlike nectin-2 and nectin-3, was partially co-localized with afadin at the OPL and IPL, in addition to the OLM (Figures 1B, S1B). Nectin-1 was co-localized with afadin in cone synapses immunostained with Arrestin3 (Arr3, cone photoreceptor marker), suggesting that puncta adherent junctions may be formed between cone pedicles and BC dendritic tips. In the postnatal day 0 (P0) retina, afadin and nectin-1 signals were observed in the outer retinal surface

where AJs are formed (Figure S1C) (Koike et al., 2005). Immunostaining with anti-afadin, anti-SCGN (Type 2-6 cone BC marker) (Puthussery et al., 2010), and anti-PKCα (rod BC marker) revealed that afadin localizes to the dendritic tips, cell bodies, and axons of ON- BCs and at least cell bodies of OFF-BCs (Figure 1D).

Afadin is required for proper retinal lamination

To investigate the role of afadin in the retina, we generated retina-specific *afadin* cKO mice by crossing *afadin flox* mice with *Dkk3-Cre* mice (Majima et al., 2009; Sato et al., 2007; Yamamoto et al., 2020). Afadin was not detected at the protein level by Western blotting in the *afadin* cKO retina (Figure S2A). The *afadin* cKO mouse was viable and showed no gross morphological abnormalities. To examine retinal lamination and morphology, using the *afadin* cKO retina at 1M, we performed toluidine blue staining. We found that there were no clear outer and inner segments of photoreceptors in the outer retina, no distinct OPL, and no clear compartmentalization of the ONL and INL (Figure 2A). Rod photoreceptors, identified by inverted nuclear architecture (Solovei et al., 2009) (Figure 2A insets), were widely scattered in the *afadin* cKO retina, whereas the IPL and GCL appeared intact. Furthermore, rosette-like structures, which lacked cell bodies centrally, were sometimes observed in the cKO outer retina (Figure 2A, B, C: arrowhead).

To investigate the defects in the OS of the cKO retina in more detail, we stained retinal sections with rhodamine-labeled peanut agglutinin (PNA, a marker of

cone photoreceptor outer segment and axon terminals) or antibodies against Rom1 (rod OS marker), Rhodopsin (rod OS marker), S-opsin (S-cone OS marker), and M-opsin (M-cone OS marker). Rhodopsin, Rom1, S-opsin, and M-opsin play central roles in phototransduction in the OS (Clarke et al., 2000; Greenwald et al., 2014; Tanimoto et al., 2015; Xu et al., 2020). Distribution of Rom1, Rhodopsin, S-opsin, M-opsin, and PNA signals in the cKO retina differed significantly from those of the *afadin* cHet retina. In the cKO retina, Rom1, Rhodopsin, S-opsin, M-opsin, and PNA signals were remarkably decreased in number and mislocalized in the retina (Figure 2B, C). These markers were not observed in the rosette-like structure of the cKO retina, suggesting that the rosette-like structure is different from the photoreceptor rosette as reported (Stuck et al., 2012). Electron microscopic analysis also demonstrated that only a few OS structures were observed between retinal cells in the disrupted ONL and INL regions of the cKO retina (Figure S2B). These findings indicate that rod and cone phototransduction may be severely impaired in the cKO retinas. To investigate the distribution of cone and rod photoreceptors in the cKO retina, we performed wholemount immunostaining with antibodies against Arr3, Rhodopsin, and Rom1. Cell bodies of cone photoreceptors were arranged regularly in the cHet retina, whereas cone photoreceptor arrangements and morphology were significantly disordered in the cKO retina (Figure 2D). Rom1, Rhodopsin, and Arr3 signals were decreased but relatively dense in some areas (Figure 2D). These data suggest that photoreceptor distribution is disrupted, but photoreceptors remain in some areas heterogeneously.

We further investigated AJs in the cKO retina by immunostaining with OLM adherens junction markers β-catenin, N-cadherin, and nectin-1. We found that these signals were dispersed in the cKO retina (Figure S2C). This data suggests that AJs in the OLM are disrupted in mature cKO retinas.

As toluidine blue staining of the cKO retina suggested mislocalization of each cell types, we investigated the position of each retinal cell body in the cKO retina by immunostaining with retinal cell type-specific markers; Otx2 (a photoreceptor and BC marker), Chx10 (a BC marker), Arr3, Calbindin (a horizontal cell and AC marker), AP2α (an AC maker), RBPMS (a RGC marker), and Lhx2 (a Müller glial cell marker) (Figure 2E). Positions of rod and cone photoreceptors, BCs, horizontal cells, and Müller glial cells were affected. In contrast, those of ACs and RGCs were relatively intact, except for the immediately surrounding region of rosette-like structures (Figure 2E). Particularly, rod and cone photoreceptors and BCs were scattered throughout the retina. Immunostaining with an anti-GS antibody (a Müller glial cell marker) showed that Müller glial cell morphology was affected, especially at the distal part. However, a distinct inner limiting membrane was retained in the cKO retina (Figure S2D). There was greater individual variation in retinal thickness, layer structure, and cell position among the cKO mice than among the cHet. These results indicate that afadin is essential for normal retinal lamination.

Ablation of afadin results in the remarkable decrease and mislocalization of photoreceptor-BC synapses

No distinct OPL structure in the cKO retina suggests that synapses between photoreceptors and BCs may be disrupted. To assess their integrity, we immunostained retinal sections of the cKO mouse (1 M) with antibodies against Bassoon (a photoreceptor synaptic ribbon marker), PSD95 (a photoreceptor synaptic terminal marker), mGluR6 (an ON-BC dendritic tip marker), GluR5 (an OFF-BC dendritic tip marker), PKCα, and PKARIIβ (a type 3b OFF cone BC marker). In the cHet retina, photoreceptor synapses containing synaptic ribbons formed a row in the OPL (Figures 3A, B, S3A). On the other hand, in the cKO retina, the row of photoreceptor synapses was not observed, and photoreceptor-BC synapses were remarkably reduced in number. Bassoon and mGluR6 were aberrantly distributed, and the position of the soma and dendritic tips of rod BCs was noticeably disturbed (Figure 3A). Only a few ribbon synapses remained (Figure 3A arrowheads). The 3D reconstructions of the confocal image stacks showed more clearly that photoreceptor ribbon synapses were decreased in number and mislocated in the cKO retina (Figure 3C, D). The contact between the axon terminal of photoreceptors and the dendrite of ON- and OFF-BCs was also significantly reduced in number, suggesting that photoreceptor-BC synapses were considerably lost in the cKO retina (Figures 3B, D, S3A, B). Along with these defects, GluR5 signals with a branch-like pattern were detected in the IPL of the cKO retina, though no GluR5 signals were found in the IPL of the cHet retina (Figure 3B, D). Photoreceptor-ON BC ribbon synapses and photoreceptor-OFF BC synapses in the outer retinal region beneath 1 mm^2 of the surface area of the cKO retina were significantly reduced to about 5% and 15% of those in the cHet retina, respectively (Figures 3E, F,

S3C). These results indicate that afadin may regulate the formation and localization of photoreceptor synapses. To investigate whether the aberrant lamination in the cKO retina can be attributed to a defect in development or maintenance, we immunostained developing cHet and cKO retinas with outer segment and photoreceptor synapse-related markers. The outer segment marker signals scattered, and the row of photoreceptor synapses was not observed in the cKO retina at P11 (Figure S3D). These data indicate that proper development of retinal lamination is impaired in the cKO retina.

Afadin is required for proper localization of GluR5 to OFF BC dendrites

GluR5, a kainate receptor subunit that forms functional homomeric and heteromeric channels, is specifically expressed in OFF BCs and localizes to their dendrites (Haverkamp et al., 2003). To investigate GluR5 localization in more detail, we immunostained the cKO retina with anti-GluR5, anti-SCGN, and anti-PKCα antibodies. We found that ectopic GluR5 signals in the IPL overlapped not only with SCGN but also PKCα in the cKO retina (Figure 4A). These data indicate that afadin may be required for specific localization of GluR5 in OFF BC dendrites. It seems likely that ectopically localized GluR5 may receive glutamate released from surrounding cells in the IPL, resulting in depolarization of ON- and OFF-BCs. It should be noted that there were no remarkable differences between cKO and cHet retinas in the localization of glutamate transporter EAAT5 and vesicular glutamate transporter vGlut1 to the axon terminal of photoreceptors and BCs (Figure 4B, C, D). It has been reported that mGluR6 localization to ON BC dendritic tips requires trans-synaptic

interaction with ELFN1 in the synaptic cleft and that ELFN1 ablation results in a remarkable reduction of mGluR6 in ON BC dendritic tips (Cao et al., 2015). As GluR5 localization may also be regulated by trans-synaptic interaction with photoreceptor synaptic terminal proteins, it seems possible that the defect of photoreceptor-OFF BC contacts prevents this trans-synaptic interaction, resulting in GluR5 mislocalization in the cKO retina.

Then, we investigated the IPL structure in the cKO retina by immunostaining it with anti-ChAT, Calbindin, and Calretinin antibodies. Distinct ON- and OFF ChAT bands, Calbindin bands, and Calretinin bands were observed in the cKO retina (Figure S3E). However, type 2-6 BCs immunostained with SCGN were slightly disturbed in the axon terminal position (Figure 4A-C). These results suggest that stratification patterns in the IPL may be slightly impaired but almost intact in the cKO retina. Immunostaining analysis with anti-HPC-1 (also known as syntaxin, an AC marker), anti-Calbindin, anti-RBPMS, and anti-Tuj1 (an RGC marker) antibodies revealed that the rosette-like structure contains AC and RGC processes inside (Figure 4E). These data indicate that the rosette-like structure in the cKO may be an ectopic IPL, termed “acellular patches” (Nahar and Cho, 2022).

Retinal cell fate is altered in the cKO retina

To examine whether afadin loss affects retinal cell fate determination, we counted the number of retinal cells immunostained with each retinal cell marker. In the cKO retina, BCs significantly increased to about 150% of the cHet retina,

but rods, cones, and Müller glial cells were significantly decreased to about 30%, 40%, and 80% of the cHet retina, respectively (Figure 4F). PKCα-positive cells and SCGN-positive cells were significantly increased (Figure S3F), indicating that both rod- and OFF-BCs were increased in the cKO retina. In contrast, the number of rod BC processes in the IPL was significantly decreased in the cKO retina (Figure S3G). Marker gene expression of photoreceptors and BCs, which showed noticeable changes in the number in 1M cKO retina, were significantly decreased and increased, respectively, in the cKO at P14, the stage when retinal cell differentiation is complete (Figure S3H). These data suggest that ectopically located bipolar cells may increase in the cKO retina. Based on these data and ectopic localization of GluR5 to ON-BCs in the cKO retina (Figure 4A), we propose that afadin may be required for normal retinal cell fate determination and gene expression. However, we cannot exclude a possibility that the decrease in photoreceptor and Müller glial cells might be due to cell death.

Small local field potentials are recorded from the cKO retina

To examine whether the cKO mouse retina can respond to light stimulation, we first recorded electoretinogram (ERG) from anaesthetized animals. Under the scotopic condition, a flash (duration; 5 ms, intensity; 1.0×10^4 cd/m^2) was applied to eyes in the dark (Figure 5A *left*). Scotopic ERG from the cHet mouse showed a negative a-wave and a following positive b-wave, whereas both waves from the cKO mouse were almost flat. Under the photopic condition, the mouse was adapted to the background light (intensity: 31.6 cd/m^2) for 10 min, then a flash (duration; 5 ms, intensity: 1.0×10^4 cd/m^2) was superimposed on the adapting

background (Figure 5A *right*). Photopic ERGs from the cHet mouse showed a small a-wave and a prominent b-wave, whereas those from the cKO mouse were almost flat. These results may be attributed to the scattered distribution of rod and cone photoreceptors, a lack of a uniform photoreceptor layer, and the decrease of outer segments and photoreceptor synapses in the cKO retina (see Figure 2).

Then, to examine whether local field potentials can be detected from the cKO retinas, we performed MEA recordings from the retinas isolated from the cKO and cHet mice. Surprisingly, a flashlight (duration; 5 ms, intensity; 2.5 x 10^4 photons/s/μm^2) could occasionally evoke micro-ERGs (mERGs) from the cKO retinas (SD of the amplitude during 300 ms after the flash onset; >50 μV, 13/590 electrodes, n = 10 retinas from 6 mice) (Figure 5B *right*). However, the amplitude of mERGs from the cKO retinas was smaller than that from the cHet retinas (SD of the amplitude during 200 ms after the flash onset; >1,000 μV, 292/413 electrodes, n = 7 retinas from 4 mice) (Figure 5B *left*). As the a-wave represents hyperpolarization of the photoreceptors and the b-wave arises from the inner retina, predominantly from ON BCs with a contribution from Müller glial cells (Perlman, 2020), the first negative and following positive waves of mERGs may correspond to the a- and b-waves, respectively. To confirm this, L-AP4, an agonist of mGluR6, was bath-applied to suppress the response of ON BCs. In the presence of L-AP4, the second positive wave disappeared, whereas the first negative wave was enhanced in the cHet retinas and remained in the cKO retinas (Figure 5B), indicating that the first negative and following positive waves

are the a- and b-waves, respectively. We compared the amplitude and implicit time (time-to-peak latency) of the a- and b-waves and found that both a- and b-waves were significantly smaller in amplitude (a-wave; cHet: 155 ± 58.7 μV, n = 292 electrodes, n = 10 retinas from 6 mice, cKO: 44.7 ± 21.7 μV, n = 13 electrodes, n = 7 retinas from 4 mice, Error bars, mean ± SD. ***$p < 0.001$, Mann-Whitney U test, b-wave; cHet: 16.3 ± 76.5 μV, n = 292 electrodes, cKO: 24.8 ± 19.6 μV, n = 13 electrodes, Error bars, mean ± SD. ***$p < 0.001$, Mann-Whitney U test) (Figure 5C) and longer in implicit time in the cKO retinas comparing to those in the cHet retinas (a-wave; cHet: 62.6 ± 10.8 ms, n = 292 electrodes, cKO: 149.0 ± 16.0 ms, n = 13 electrodes, Error bars, mean ± SD. ***$p < 0.001$, Mann-Whitney U test, b-wave; cHet: 127.0 ± 25.3 ms, n = 292 electrodes, cKO: 229.0 ± 60.7 ms, n = 13 electrodes, Error bars, mean ± SD. ***$p < 0.001$, Mann-Whitney U test) (Figure 5E). The ratio of b-wave amplitude to a-wave amplitude (b/a) was significantly smaller in the cKO retinas than that in the cHet retinas (cHet; 1.19 ± 0.67, cKO; 0.59 ± 0.23, Error bars, mean ± SD. ***$p < 0.001$, Mann-Whitney U test) (Figure 5D), suggesting that the efficiency of synaptic transmission from photoreceptors to ON BCs may be decreased in the cKO retinas. However, difference of the implicit time between a- and b-waves was similar in the cKO and cHet retinas (cHet; 64.4 ± 22.0 ms, cKO; 80.4 ± 50.9 ms, $p = 0.40$, Mann-Whitney U test) (Figure 5F), suggesting that signals from photoreceptors to ON BCs may be transmitted properly. These results indicate that despite severe disorganization of the cKO outer retina, photoreceptors can still respond to light stimulation and that the synaptic transmission from photoreceptors to ON-BCs remains functional.

RGCs in the cKO retinas evoke firings to light stimulation

Using the MEA system, we recorded spike discharges from RGCs in retinas isolated from the cKO and cHet mice. The frequency of spontaneous firings in the dark was not different significantly between cKO and cHet retinas (cHet; 12.5 ± 19.2 Hz, n = 434, cKO; 10.8 ± 14.6 Hz, n = 388, p = 0.79, Mann-Whitney U test). We examined whether RGCs in the cKO retina respond to light stimulation. The isolated retina was stimulated by a flash (duration; 2 s, intensity; 24.2 or 27.3 cd/m^2) seven times every 8 s, and the PSTH was calculated for each RGC after spike sorting. RGCs could be classified into “ON”, “ON-OFF”, “ON-OFF inhibition”, “OFF”, and “None” types (Figure 6A, B; see **MATERIALS and METHODS**). All types were found in both cKO and cHet retinas, and the composition of RGC types was similar in both retinas (Figure 6C). We also investigated whether RGCs received both rod and cone inputs and found that > 60 % of RGCs among successfully spike sorted RGCs in both the cKO and cHet retinas received both inputs (Figure 6D).

Receptive fields are characterized in some RGCs

Using pseudorandom checkerboard pattern stimulation, we examined the properties of spatiotemporal RF of RGCs by calculating the spike-triggered average. Amazingly, we could identify RFs in the cKO retina. To check the morphology of the retina where RFs were identified, the retina was removed from MEA after recording, and sliced retinal sections were immunostained with anti-PKARIIβ, anti-PSD95, and anti-PKCα antibodies (Figure 7A). The sectioned

region clearly showed impairment of the outer retina, where it was difficult to identify or locate photoreceptors. On the other hand, the inner retina was apparently normal, and both INL and IPL could be recognized. Even though the outer retina was severely impaired, we could identify RF of RGCs (Figure 7B). However, the cells with clear RF were fewer in the cKO retinas (69/388 cells, n = 4 retinas) than those in the cHet retinas (195/434 cells, n = 4 retinas). By fitting ellipse to each RF, we measured the short and long axes and calculated the RF area (Figure 7C, D, E). The RF area in the cKO retinas was significantly smaller than that in the cHet retinas (cHet; 0.0307 ± 0.0210 mm^2, n = 195, n = 4 retinas, cKO; 0.0161 ± 0.00839 mm^2, n = 69, n = 4 retinas, Error bars, mean ± SD. ***p < 0.001, Mann-Whitney U test). We tried to find an antagonistic surround of RFs, but it was difficult to detect a clear surround in both cKO and cHet retinas.

The temporal profile of RFs was calculated, and the principal component analysis was performed. Then, using UMAP for clustering, we could recognize 5 clusters (Figure 7F, cKO; n = 4 retinas, cHet; n = 4 retinas). The temporal profile belonged to each cluster was superimposed separately (Figure 7G). Among 5 clusters, clusters 1 and 2 did not include the temporal profiles calculated from RGCs in the cKO retinas. The temporal profiles of cluster 1 and cluster 2 were ON and OFF types, respectively, each of which had a shorter time-to-peak latency (cluster 1; -113 ± 15 msec, n = 31, cluster 2; -111 ± 13 msec, n = 36) comparing to the other temporal profiles obtained from RGCs in both cKO and cHet retinas (cHet; cluster 3; -200 ± 31 msec, n = 51, cluster 4; -171 ± 19 msec, n = 37, cluster 5; -178 ± 28 msec, n = 40, cKO; cluster 3; -163 ± 21 msec, n = 10,

cluster 4; -238 ± 34 msec, n = 36, cluster 5; -217 ± 41 msec, n = 23). These results indicate that the light-evoked responses of RGCs in the cKO retina are not as refined as cHet. Actually, the rising time of transient responses (determined by a upward deflection soon after light stimulation obtained from the cumulative curve of each PSTH) was significantly longer in the cKO retina (58.5 ± 19.8 ms, n = 17) than in the cHet retina (43.0 ± 17.8 ms, n = 23) (***$p < 0.001$, Student's test).

It has been reported that degenerated retinas, such as the *rd1* retinas (Poria and Dhingra, 2015), show oscillatory spontaneous firings in RGCs. Thus, we checked whether RGCs in the cKO retina show RGC oscillations. RGCs in the cKO retinas showed oscillations (P30; 1.55 % of 382 RGCs, 14.0 ± 2.4 Hz, n = 4 retinas, P40, 15.0 % of 333 RGCs, 9.2 ± 3.8 Hz, n = 4 retinas). On the other hand, RGCs in the cHet retinas did not show obvious RGC oscillations (0 % of 432 RGCs, n = 4 retinas).

Ectopic AJs and aberrant localization of mitotic cells are observed in the *afadin* cKO retina

As RGC oscillations were observed in the cKO retina, like the *rd1* retinas with photoreceptor degeneration (Choi et al., 2014), we examined whether RGC oscillations were related to cell death in the cKO retina. Using anti-active caspase3 (an apoptotic cell marker), we counted the number of dead cells immunohistochemically. We found that dead cells were significantly increased in the cKO retina at around P30 (Figure 8A, B). Photoreceptors in the cKO retinas

were already decreased to less than 30% of the cHet retinas at around P30 (Figure 4F). These findings suggest that the progressive cell death observed in the cKO retina may lead to a further decrease of photoreceptors, resulting in an increase of oscillatory RGCs at P40.

We previously demonstrated that the photoreceptor-cell specific *aPKCλ* KO retina shows disruption of AJs and mislocalization of mitotic progenitors in developing stage, followed by severe lamination defects in adults (Koike et al., 2005). In the developing retina, AJs are observed in the outer retinal surface, where progenitor cells divide and migrate toward the inner retina. To investigate the possibility that disruption of AJs may lead to abnormal cell migration and lamination, we immunostained the cKO retina at P0 with anti-β-catenin, N-cadherin, nectin-1, and phospho-histone H3S10 (pHH3, a marker of the mitotic cell) (Figure 8C). N-cadherin, nectin-1, and β-catenin signals were obviously detected, but these signals were localized in the inner retina with aberrant patterns. These signals were slightly observed in the outer retina. These results indicate that ectopic AJs are present in the cKO retina. Mitotic cells immunostained by pHH3 were localized near the ectopic AJs, suggesting that progenitor cells may divide in an ectopic location and migrate aberrantly in the cKO retina, resulting in lamination defects.

DISCUSSION

In the current study, we showed that the *afadin* cKO retina exhibits various severe pathological defects, including photoreceptor morphological defects,

mislocalization, reduced photoreceptors and its synapses, disruption of outer retinal lamination, ectopic localization of GluR5, aberrant rosette-like structure in the outer retina (Figures 2-4). These results suggest that afadin is required for normal retinal lamination, photoreceptor cell morphology, photoreceptor synapse formation, and proper GluR5 localization to OFF bipolar cell dendrites. Conditional loss of AJ molecules in the retina has been reported to cause partial or complete disruption of retinal lamination (Erdmann et al., 2003; Fu et al., 2006; Masai et al., 2003). However, the effect of AJ molecule loss on the retinal cell morphology and synapses was unclear. We revealed that loss of afadin significantly reduces photoreceptor synapses overall, but some synapses remain.

In the *afadin* cKO mouse retina with severe outer retinal disorganization, we detected the a- and b-waves of mERG and the RF of RGCs. These results suggest that some visual information processing may be performed by newly formed and preserved circuits even when the retinal structure is severely impaired and the photoreceptor is remarkably decreased in number. To our knowledge, this is the first report that the RF of RGCs could be formed if several functional photoreceptors connect to BCs, even when the outer retinal lamination is severely disrupted (Figure 7). The number and size of RFs observed in the cKO retina were smaller than those in the cHet retina, suggesting that the precise arrangement of retinal cells and lamination is necessary for normal visual function. It is important to note that light stimulation evoked firing responses in RGCs around the rosette-like structure, and that such

RGC firings could not be detected by a large distance between RGC soma and MEA electrode.

We would like to speculate why the RF of RGCs was observed in the *afadin* cKO retina. First, visual processing may be partially preserved without any remodeling if only a small number of functional photoreceptor-BC-RGC pathways remain intact. It has been shown that the RF of RGCs is detected even when approximately half of cone photoreceptors are stimulated (Care et al., 2019; Lee et al., 2022). Thus, in the *afadin* cKO retina, where cone photoreceptors are reduced to about 40% of the cHet retina, such reduction *per se* may not critically affect the RF organization. A few photoreceptor-BC-RGC pathways (vertical pathways of the retina) are inferred to be maintained in the cKO retina. In some regions, the density of photoreceptors was high enough to make functional synapses between photoreceptor and BC (Figure 2D), possibly resulting in the RF of RGCs. Second, synaptic rewiring of interneurons such as BCs may recover retinal function in the *afadin* cKO retina. Various studies show partial loss of photoreceptors or BCs, or partial silencing of BCs causes rewiring in the developing and mature retina (Johnson and Kerschensteiner, 2014; Jones et al., 1995; Okawa et al., 2014; Shen et al., 2020; Strettoi et al., 2022). Also, in the *rd1* retina, neural connections between inner retinal neurons via gap junctions may be enhanced, potentially resulting in the widespread distribution of electrically evoked RGC responses (Ahn et al., 2022). These reports suggest that reduced input from photoreceptors and BCs may lead to synaptic reorganization among surviving cells. It is possible that synaptic reorganization

triggered by reduced photoreceptor and BC inputs may occur in the *afadin* cKO retina with severe defects of the photoreceptor synapses and outer segments in the developing stages, and that this might contribute to RF formation. Synaptic rewiring may occur between BC dendrites and their closely located photoreceptor terminals in the cKO retina. It may be necessary to count the number of BC dendritic connections to each cone pedicle to verify the synaptic rewiring between photoreceptor and BC, but this was quite difficult because of the remarkably aberrant cone morphology in the cKO retina. As the IPL was relatively intact and BC axon terminals were surrounded by many RGC dendrites, synaptic reconnections between BC axon terminals and RGC dendrites are presumed to be more easily established than those between photoreceptor terminals and BC dendrites in the cKO retina. Thus, several BCs connected with multiple functional photoreceptors may rewire to RGC dendrites and transmit signals efficiently. Our findings imply that a very few BCs receiving input from functional photoreceptors responded to light stimulation, and that the output signal can be amplified downstream. The above two possibilities could both contribute to the formation of RGC RFs. Furthermore, we cannot rule out a possibility that gene expression may be changed in the *afadin* cKO retina, resulting in facilitation of RF formation.

The ratio of responding to non-responding RGCs to light stimulation in the *afadin* cKO retina was comparable to that in the cHet retina despite notable reduction of photoreceptors (Figures 4F, 5, 6). It seems likely that the number of photoreceptors connected to spreading dendrite tips of one BC may be

increased, and that glutamate spillover from BC terminals may contribute to increase the responsiveness of RGCs in the cKO retina because glutamate transporter EAAT5 and vesicular glutamate transporter vGlut1 were similar in both cKO and cHet retinas (Figure 4B-D). Glutamate released from BC terminals may spread and bind GluR5 ectopically localized in BC processes in the IPL, enhancing the response and expanding the responding area (Figure 4). These factors may contribute to emergence of RF, but the RF size in the cKO retina was still smaller than that in the cHet retina (Figure 7). Photoreceptors in the cKO retina were reduced to 30 to 40% of the cHet retina and scattered (Figures 2, 4F). The random checkerboard pattern used for STA was projected onto the assumed photoreceptor layer of the normal retina. However, as the morphology and position of photoreceptors were disturbed in the cKO retina (Figures 2, S2B), the remaining photoreceptors would be stimulated by a blurred image with decreased intensity. Accordingly, photoreceptors possibly responded weakly to blurred images, and thresholding of noise (increment >+4 SDs, decrement <-2 SDs, determined by the spontaneous firing rate, see **MATERIALS and METHODS**) may result in reduction of the RF size. Rod-driven responses were observed in RGCs in the cKO retina (Figures 5, 6). However, it is unlikely that the rod transmits signals to cones through gap junctions in the disrupted cKO outer retina, and thus, rod signals may not be transmitted to RGCs via the traditional AII amacrine-ON cone BC pathway.

The temporal profile of RFs in the cKO retina did not include that with short time-to-peak latency (Clusters 1 and 2; Figure 7), indicating that RGCs in the

cKO retina cannot respond to rapid changes in luminance. There are several possibilities to explain this result. For example, disruption of the outer retinal lamination may make it difficult to synchronize photoreceptor responses without gap junctions, resulting in dulled responses. BCs with fast response kinetics may not be present or not functional in the cKO retina (Kuo et al., 2024). Furthermore, glutamate spillover from BC terminals may amplify the signals, but at the same time, the time-to-peak of RGC responses may be delayed. These possibilities should be investigated in the future.

Ectopic continuous AJs formed in the developing *afadin* cKO retina (Figure 8C) are possibly associated with partial disruption of retinal lamination. The *β-catenin* cKO retinas also show ectopic continuous AJs in developing stage and the disruption of the outer retinal lamination with relatively intact IPL and GCL structure in adult (Fu et al., 2006), suggesting that afadin and β-catenin are required for normal continuous AJ formation at the outer retinal surface but dispensable for maintaining AJs. The photoreceptor-specific *aPKCλ* cKO retina in which AJs are dispersed in the developing stage exhibits disruption of whole retinal lamination despite aPKCλ remaining in cells excluding photoreceptors. Individual cells contain AJs, but the AJs are not continuous in the *aPKCλ* cKO retina (Koike et al., 2005). These findings, based on the studies using each mutant mouse, imply that continuous AJs are important for the formation of the outer retinal structure.

In the *afadin* cKO retina, significant increase in BCs and significant decrease in

photoreceptors and Müller glial cells were observed at 1M (Figures 4F, S3F). In particular, the changes in the numbers of photoreceptors and BCs were remarkable, and it was consistent with the expression change of their marker genes in the developing cKO retina (Figure S3H). These results suggest that retinal cell fate was affected in the *afadin* cKO mice. As retinal cell fate is not altered in the *β-catenin* cKO retina (Fu et al., 2006), the phenotypic difference between *β-catenin* cKO and *afadin* cKO retinas may imply distinct functional properties of the in AJ molecules.

One of the major concerns of retinal regeneration therapy is that while transplanted photoreceptors can form synapses with donor BCs, the transplanted tissue often shows aberrant structures, such as rosettes (Yamasaki et al., 2022). Our study demonstrated that RGCs show RFs even if the outer retinal lamination is disrupted, but synapse formation is maintained to a certain extent. Therefore, retinas with transplant surgery might recognize stimulus patterns to some extent, even if aberrant structures are formed after retinal transplantation, and retinal regeneration therapy could be more effective in restoring vision than previously anticipated. Although RFs of RGCs were observed in the *afadin* cKO mouse, some mice exhibited visual impairments despite RFs being observed, such as mice with partial cone photoreceptor ablation in the mature stage (Care et al., 2019; Shen et al., 2020). Further analyses that evaluate various visual functions are needed to determine how much vision remains in the cKO mouse.

Acknowledgments

We thank Dr. Takahisa Furukawa for providing *Dkk3*-Cre mice, Takefumi Yamamoto for technical assistance in electron microscopy, Drs. Akishi Onishi and Kiyo Sakagami for helpful comments, and Y. Shibata for technical assistance.

Funding

This work was supported by Grant-in-Aid for Scientific Research (B) (24390019), Fund for the Promotion of Joint International Research (22KK0137), Early-Career Scientists (23K15920), and Research Activity Start-up (22K20698) from the Japan Society for the Promotion of Science (JSPS), Takeda Science Foundation, the Kobayashi Foundation, JST PRESTO (08062795), and R-GIRO.

Author Contributions

C.K., M.T., and A.G.U. designed the project. Y.T. and J.M. generated *afadin flox* mice. A.G.U. and H.T. carried out immunohistochemical analysis. A.G.U. performed molecular biochemical analyses. T.K. performed electron microscopic analysis. H.O. and S.M. carried out ERG experiments. H.O. and M.W. performed multi-electrode recordings. K.S., T.N., and M.T. analyzed data of the multi-electrode recordings. A.G.U., M.T., and C.K. wrote the manuscript. C.K. supervised the project.

FIGURE LEGENDS

Figure 1. Afadin is localized to the OS, OLM, OPL, INL, and IPL.

A. Immunostaining of the wild-type (WT) mouse retina (1M) with anti-afadin antibody. The afadin signals disappeared in the pre-absorbed (peptide+) sample. Nuclei were stained with DAPI (blue).

B. Immunostaining of the WT retinal section (1M) using anti-afadin (green) combined with anti-Nectin-1 (red) antibody. Necin-1 was partially co-localized with afadin in the OLM, OPL, and IPL. Nectin-2 and nectin-3 were localized only in the OLM.

C. Afadin was colocalized with nectin-1, nectin-2, and nectin-3 at the OLM. The 1M WT retinal sections were immunostained with anti-afadin (green), anti-nectin-1 (red, upper panels), anti-nectin-2 (red, middle panels), and anti-nectin-3 (red, lower panels) antibodies.

D. Immunostaining of 1M WT retinal sections using anti-afadin (green), anti-SCGN (red), and anti-PKCα(white) antibodies. Afadin signals overlapped with SCGN and PKCα in the OPL and INL and PKCα in the IPL.

OS, the outer segment; IS, the inner segment; OLM, the outer limiting membrane; ONL, the outer nuclear layer; OPL, the outer plexiform layer; INL, the inner nuclear layer; IPL, the inner plexiform layer; GCL, the ganglion cell layer.

Figure 2. Outer retinal lamination is severely disrupted in the *afadin* cKO retina.

A. Toluidine blue staining of the cHet and cKO mouse retinal sections at 1M. The retinal layer structure was disrupted in the cKO retina. Rod photoreceptor nuclei (insets) were deeply stained. The red asterisk indicates rod photoreceptor. The arrowhead indicates a rosette-like structure. Scale bar in the inset, 2.5 μm.

B. Representative images of the cHet and cKO retinas (1M) stained with anti-Rom1 (green) and anti-Rhodopsin (Rho, red) antibodies and PNA-rhodamine (white). Rom1, Rhodopsin, and PNA signals were remarkably decreased and scattered in the cKO mice. The arrowhead indicates the rosette-like structure.

C. Representative images of the cHet and cKO retinas (1M) stained with anti-S-opsin (green) and anti-M-opsin (white) antibodies and PNA-rhodamine (red). Cone OSs were aberrantly located in the cKO retina. The arrowhead indicates the rosette-like structure.

D. Retinal flat-mount immunostaining of the cHet and cKO retinas immunostained with anti-Arr3 (green, left panels), anti-Rom1 (green, right panels), and anti-Rhodopsin (red, right panels) antibodies. The inset shows an area with a relatively high density of photoreceptors in the cKO retina.

E. Immunofluorescent analysis of the cHet and cKO retinas (1M) using anti-Arr3 (cone marker, green in the left panels), anti-Otx2 (photoreceptor and BC marker, red in the left panels), anti-RNA binding protein with multiple splicing (RBPMS, RGC marker, green in second left panels), anti-Chx10 (BC marker, red in second left panels), anti-Lhx2 (Müller glia marker, green in third left and third right panels), anti-AP2α (AC marker, red in third left and second right panels), and anti-Calbindin (horizontal cell and AC marker, white in third left and right panels)

antibodies. Arrowheads indicate RGCs and ACs near the rosette-like structure.

Figure 3. Photoreceptor-BC synapses were severely impaired and mislocalized in the *afadin* cKO retina.

A. Immunostaining of the cHet and cKO retinal sections at 1M with anti-Bassoon (green), anti-mGluR6 (red), and anti-PKCα (white) antibodies. The arrowhead indicates the synapse between rod and rod-BC.

B. Immunostaining of the cHet and cKO retinas at 1M with anti-GluR5 (green), anti-PSD95 (red), and anti-PKARIIβ (white) antibodies. The arrowhead indicates the synapse between the cone and OFF-BC.

C. 3D projection of confocal image immunostaining with anti-Bassoon (green), anti-mGluR6 (red), and anti-PKCα (white) using the cHet and cKO retina (1M). The inset shows the synapse between the rod and BC at high magnification. The arrowhead indicates the ribbon synapse between rod and rod-BC.

D. 3D projection of confocal image immunostaining with anti-GluR5 (green), anti-PSD95 (red), and anti-PKARIIβ (white) antibodies using the cHet and cKO retina (1M).

E. Quantification of the number of synapses between rod photoreceptor and rod-BC under 1mm2 of retinal surface in the cHet and cKO mice immunostained with anti-Bassoon, anti-mGluR6, and anti-PKCα antibodies (cHet; 599.6 ± 49.7, n = 3, cKO; 29.1 ± 12.75, n = 4, 10 images from each mouse. Error bars, mean ± SD. ***$p < 0.001$ by Student's t test). The number of synapses decreased to about 5 % of the cHet in the cKO retina.

F. Quantification of the number of synapses between photoreceptor cells and

type 3 OFF-BC under 1mm^2 of the retinal surface in the cHet and cKO mice immunostained with anti-GluR5, anti-PSD95, and anti-PKARIIβ antibodies (cHet; 24.0 ± 2.8, n = 3, cKO; 4.1 ± 1.3, n = 3, 10 images from each mouse. Error bars, mean ± SD. ***p < 0.001 by Student's t-test). The number of synapses between the photoreceptor and Type 3 OFF-BC was decreased to about 15 % of the cHet in the cKO retina.

Figure 4. GluR5 is ectopically localized to ON and OFF BC processes.

A. Immunostaining of the cHet and cKO retinal sections at 1M with anti-GluR5 (green), anti-SCGN (red), and anti-PKCα antibodies. Obvious GluR5 signal was observed in the IPL of the cKO retina. Yellow and white arrowheads indicate overlap of GluR5 and PKCα, and GluR5 and SCGN, respectively.

B. Representative images of immunostained cHet and cKO retinas (1M) with anti-GluR5 (green), anti-vGlut1 (red), and anti-SCGN (white) antibodies.

C, D. The cHet and cKO retinas (1M) stained with anti-EAAT5 (green), anti-SCGN (red in **C**), and anti-PKCα (white in **C**), anti-PSD95 (red in **D**) antibodies and PNA-rhodamine (white in **D**). Glutamate transporter EAAT5 localization to ON and OFF BC axon terminals and photoreceptor axon terminals were unaffected in the cKO retina.

E. Immunofluorescent analysis of the cHet and cKO retinas (1M) with anti-HPC-1 (AC marker, green in the left panels), anti-Calbindin (red in the left panels), anti-Tuj1 (RGC marker, green in the right panels), and anti-RBPMS (red in the right panels) antibodies.

F. The number of each retinal cell types per 100 μm width of retinal section

(cHet; rod 185.9 ± 17.5, cone 8.4 ± 1.4, BC 45.5 ± 5.2, horizontal cell 2.1 ± 0.4, AC 30.1 ± 3.2, RGC 7.4 ± 1.5, Müller glial cell 15.7 ± 2.3, n = 4, cKO; rod 57.3 ± 17.3, cone 3.5 ± 1.3, BC 64.6 ± 7.8, horizontal cell 1.9 ± 0.7, AC 27.6 ± 6.3, RGC 5.7 ± 0.9, Müller glial cell 12.4 ± 1.5, n = 4. Error bars, mean ± SD. Horizontal cell $p = 0.58$, AC $p = 0.52$, RGC: $p = 0.10$. ***$p < 0.001$, **$p < 0.001$, *$p < 0.05$ by Student's t test). Rod and cone photoreceptors and Müller glial cells were significantly decreased to about 30, 40, and 80% of the cHet retina, respectively, and BCs were significantly increased to about 150% of the cHet retina in the cKO retina.

Figure 5. Reduction of the a- and b-waves in the *afadin* cKO retina.

A. *Left*, Scotopic ERGs from anesthetized cHet (n = 3; black) and cKO (n = 3; magenta) mice. A flash (duration; 5 ms, white LED, intensity; 1.0×10^4 cd/m^2) was applied to eyes in the dark three times. Traces: averaged (dark) and SD (pale). *Right*, Photopic ERGs. Anesthetized cHet (black) and cKO (magenta) mice were light (31.6 cd/m^2) adapted for 10 min, and then, a flash (duration; 5 ms, intensity; 1.0×10^4 cd/m^2) was superimposed on the adapted light to eyes 16 times.

B. mERGs recorded by MEA from the cHet (black) and cKO (magenta) retinas. A flash (duration; 5 ms, green LED; λ_{max} = 510 nm, intensity; 2.5×10^4 photon/s/μm^2) was applied to the isolated whole retina 3 times every 10 s. Control (solid line), L-AP4 (10 μM) (pale), and after washout (dotted line).

C. *Left*, Amplitude of the a-wave (cHet; 155 ± 58.7 μV, n = 292 electrodes, cKO; 44.1 ± 21.7 μV, n = 13 electrodes, Error bars, mean ± SD. ***$p < 0.001$,

Mann-Whitney U test). *Right*, Amplitude of the b-wave (cHet; 163 ± 76.5 μV, n = 292 electrodes, afadin cKO; 28.4 ± 19.6 μV, n = 13 electrodes, $p = 7.08 \times 10^{-09}$, Mann-Whitney U test).

D, Ratio of b-wave amplitude / a-wave amplitude (b / a) (cHet; 1.19 ± 0.67, cKO; 0.59 ± 0.23, Error bars, mean ± SD. ***$p < 0.001$, Mann-Whitney U test).

E, *Left*, Implicit time of the a-wave (cHet; 62.6 ± 10.8 ms, n = 292 electrodes, cKO; 149 ± 16.0 ms, n = 13 electrodes, $p = 5.34 \times 10^{-10}$, Mann-Whitney U test). *Right*, Implicit time of the b-wave (cHet; 127 ± 25.3 ms, n = 292 electrodes, cKO; 229 ± 60.7 ms, n = 13 electrodes, Error bars, mean ± SD. ***$p < 0.001$, Mann-Whitney U test).

F, Difference between implicit time of the b-wave and that of the a-wave (cHet; 64.4 ± 22.0 ms, n = 292 electrodes, cKO; 80.4 ± 50.9 ms, n = 13 electrodes, Error bars, mean ± SD. $p = 0.40$, Mann-Whitney U test).

Figure 6. RGC classification based on the light-evoked responses.

A, B. Light-evoked responses. **A**, cHet. **B**, cKO. A flash (duration; 2 s, intensity; 24.2 or 27.3 cd/m^2) was applied seven times every 8 s. After spike sorting, the raster plots (top) and the PSTHs (bottom) were created (20 ms/bin). Based on the PSTHs, RGC responses were classified into “ON”, “ON-OFF”, “ON-OFF inhibition”, “OFF”, and “None” types.

C. Ratio of responded to non-responded types (cHet; n = 434, n = 4 retinas, cKO; n = 388, n = 4 retinas).

D. Rod and cone inputs to RGCs (cHet; n = 434, n = 4 retinas, cKO; n = 388, n = 4 retinas). 2-s green LED flash (λ_{max} = 510 nm, intensity; 4.8×10^3

photons/s/μm^2) and UV LED flash (λ_{max} = 360 nm, intensity; 3.3 x 10^4 photons/s/μm^2) were applied 7 times every 8 s to stimulate mainly rods and S cones, respectively.

Figure 7. Spatiotemporal properties of the RF of RGCs.

A. *Left*, An isolated retina on the MEA. Electrodes (black square) mapped receptive fields (colored oval), and the region (magenta square) where immunohistochemical examination was performed after recording. Scale bar 200 μm. *Right*, Immunohistochemical staining with anti-PKARIIβ (green), anti-PSD95 (red), and anti-PKCα (white) antibodies. IPL: the inner plexiform layer.

B. Number of cells whose RF was clearly observed (cHet; 195/434 cells, n = 4 retinas, cKO; 69/388 cells, n = 4 retinas).

C. The spatial profile of RFs in the cHet (*Top*) and cKO (*Bottom*) retinas. Color scale illustrates high (red) to low (blue) relative to the average (green). Scale bar 100 μm.

D. RF size of the cKO retina was significantly smaller than that of the cHet retina (cHet; 0.0307 ± 0.0210 mm^2 n = 195, n = 4 retinas, cKO; 0.0161 ± 0.00839 mm^2 n = 69, n = 4 retinas, Error bars, mean ± SD. ***p < 0.001, Mann-Whitney U test).

E. Short and long axes of the oval fitted to each RF.

F. Clustering of RGCs based on the temporal profile of RFs. Five clusters were visualized (cHet; circle, cKO; x).

G. Temporal profiles from each cluster were superimposed separately (cHet; black, cKO; magenta, mean; solid line, SD; pale line).

H. Time-to-peak latency of the temporal profile (cHet; filled bar, cKO; open bar).

Mean ± SD. (cHet; cluster 1; -113 ± 15 msec, n = 31, cluster 2; -111 ± 13 msec, n = 36, cluster 3; -200 ± 31 msec, n = 51, cluster 4; -171 ± 19 msec, n = 37, cluster 5; -178 ± 28 msec, n = 40, cKO; cluster 3; -163 ± 21 msec, n = 10, cluster 4; -238 ± 34 msec, n = 36, cluster 5; -217 ± 41 msec, n = 23).

Figure 8. Ectopic AJs are observed in the developing *afadin* cKO retina.

A. Immunostaining of the cHet and cKO retinas (1M) with anti-active caspase 3 (AC3, green) antibody. Arrowhead indicates AC3 positive cell.

B. Quantification of apoptotic cells per $1mm^2$ in the cHet and cKO retinas at 1M (cHet; 0.6 ± 0.7, n = 4, cKO; 66.7 ± 18.2, n = 5). Apoptotic cells were significantly increased in the cKO retina. Error bars, mean ± SD. ***$p < 0.001$ by Student's t-test.

C. Immunostaining of the cHet and cKO retinas at postnatal day 0 (P0) with anti-phospho-histone H3S10 (pHH3, mitotic cell marker, green), anti-N-Cadherin (red in left, second left, and second right panels), anti-Nectin-1 (white in left, second left, and third right panels), anti-β-catenin (red in the right panels) antibodies. Ectopic N-cadherin, nectin-1, and β-catenin signals were observed inside the cKO retinas, and pHH3-positive cells were localized near these ectopic signals.

Figure S1. Afadin is localized to AJs in the developing and mature retinas.

A. Immunostaining of the WT retinal section (1 M) with anti-afadin (green) antibody combined with nectin-2 (red, upper panels) and nectin-3 (red, upper panels) antibodies.

B. Immunostaining with anti-afadin (green), anti-nectin-1 (red), and anti-Arr3 (a cone marker, white) antibodies. Afadin was co-localized with nectin-1 in cone synapses.

C. Immunostaining of the WT retinal section (P0) with anti-afadin (green) and anti-nnectin-1 (red) antibodies.

Figure S2. The OLM AJs are disrupted in the afadin cKO retina.

A. Western blot analysis of the cHet and cKO retinas using anti-afadin (upper panel) and anti-GAPDH (lower panel) antibodies. No significant afadin band was detected in the cKO retina.

B. Electron microscopic analysis of the cHet and cKO retinas (1M). A few ectopic disc structures were observed in the cKO retina. The inset shows the ectopic disc structure at high magnification. The arrowhead indicates the outer segment disc structure.

C. Immunostaining of the cHet and cKO retinal sections at 1M using anti-β-catenin (green, left panels), anti-nectin-1 (red, left panels), and anti-N-cadherin (green, right panels). Signals of these markers were not observed at the outer retinal surface in the cKO mice.

D. Immunostaining of the cHet and cKO retinal sections at 1M using anti-glutamine synthetase (GS, green) antibody. Obvious GS signals were observed in the inner side of the cKO retina but not at the outer retinal surface in the cKO mice.

Figure S3. The OS and photoreceptor-BC synapses are affected in the

developing afadin cKO retina.

A. Immunostaining of the cHet and cKO retinas at 1M with anti-PKCα (green), anti-PSD95 (red) antibodies.

B. 3D projection of confocal image immunostaining with anti-PKCα (green), anti-PSD95 (red) antibodies.

C. Quantification of the number of contacts between photoreceptor and rod ON-BC under 1mm^2 of retinal surface in the cHet and cKO mice immunostained with anti-GluR5, anti-PSD95, and anti-PKARIIβ antibodies (cHet; 550.5 ± 29.1, n = 3, cKO; 65.2 ± 7.9, n = 3, 10 images from each mouse. Error bars, mean ± SD. ***$p < 0.001$ by Student's t-test). The number of synapses between the rod and ON BC was decreased to about 10 % of the cHet in the cKO retina.

D. Representative images of the cHet and cKO retinas (P11) stained with antibodies against Rom1 (green, left panels), Rhodopsin (white, left panels), PKARIIβ (green, middle panels), Arr3 (red, middle panels), Bassoon (green, right panels), mGluR6 (red, right panels), PKCα (white, right panels). The inset shows the synapse between Cones and Type 3 OFF-BCs (middle panels) and ribbon synapses (right panels) at high magnification.

E. Immunostaining of the cHet and cKO retinal sections at 1M with anti-ChAT (green), anti-Calretinin (red), and anti-Calbindin (white) antibodies. Obvious ChAT bands, Calretinin bands, and Calbindin bands were observed in the IPL of the cKO mice.

F. The number of PKCα+ and SCGN+ cells per 100 μm width of retinal section (cHet; PKCα+ 15.8 ± 2.6, SCGN+ 24.7 ± 4.8, n = 4, cKO; PKCα+ 23.6 ± 5.2, SCGN+ 37.4 ± 7.7, n = 4. Error bars, mean ± SD. *$p < 0.05$ by Student's t-test).

PKCα+ cells and SCGN+ cells were significantly increased to 150% of the cHet.

G. The number of PKCα+ cell processes in the IPL per 100 μm width of retinal section (cHet; 18.6 ± 0.5, n = 4, cKO; 14.7 ± 1.2, n = 4. Error bars, mean ± SD. ***$p < 0.01$, *$p < 0.05$ by Student's t-test). The number of PKCα+ cell processes was significantly decreased to 150% of the cHet.

H. Expression of photoreceptor and BC marker genes in the cHet and cKO at P14 (Nrl and Rhodopsin; rod marker, Opnsw and Opnmw; cone maker, Trpm1 and mGluR6; ON BC marker, Chx10; BC marker). Each gene expression was normalized by GAPDH, a house keeping gene. Expression of Nrl, Rhodopsin, Opnsw, and Opnmw were significantly decreased and those of mGluR6, Trpm1, and Chx10 were significantly increased in the cKO retina. Error bars, mean ± SD. ***$p < 0.001$, ***$p < 0.01$ by Student's t-test.

REFERENCES

Ahn J, Cha S, Choi K-E, Kim S-W, Yoo Y, Goo YS. 2022. Correlated activity in the degenerate retina inhibits focal response to electrical stimulation. *Front Cell Neurosci* **16**:889663.

Amini R, Rocha-Martins M, Norden C. 2017. Neuronal migration and lamination in the vertebrate retina. *Front Neurosci* **11**:742.

Ayala R, Shu T, Tsai L-H. 2007. Trekking across the brain: the journey of neuronal migration. *Cell* **128**:29–43.

Baum B, Georgiou M. 2011. Dynamics of adherens junctions in epithelial establishment, maintenance, and remodeling. *J Cell Biol* **192**:907–917.

Cao Y, Sarria I, Fehlhaber KE, Kamasawa N, Orlandi C, James KN, Hazen JL, Gardner MR, Farzan M, Lee A, Baker S, Baldwin K, Sampath AP, Martemyanov KA. 2015. Mechanism for selective synaptic wiring of rod photoreceptors into the retinal circuitry and its role in vision. *Neuron* **87**:1248–1260.

Care RA, Kastner DB, De la Huerta I, Pan S, Khoche A, Della Santina L, Gamlin C, Santo Tomas C, Ngo J, Chen A, Kuo Y-M, Ou Y, Dunn FA. 2019. Partial cone loss triggers synapse-specific remodeling and spatial receptive field rearrangements in a mature retinal circuit. *Cell Rep* **27**:2171-2183.e5.

Choi H, Zhang L, Cembrowski MS, Sabottke CF, Markowitz AL, Butts DA, Kath WL, Singer JH, Riecke H. 2014. Intrinsic bursting of AII amacrine cells underlies oscillations in the rd1 mouse retina. *J Neurophysiol* **112**:1491–1504.

Clarke G, Goldberg AF, Vidgen D, Collins L, Ploder L, Schwarz L, Molday LL, Rossant J, Szél A, Molday RS, Birch DG, McInnes RR. 2000. Rom-1 is required for rod photoreceptor viability and the regulation of disk morphogenesis. *Nat Genet* **25**:67–73.

de Ligt J, Willemsen MH, van Bon BWM, Kleefstra T, Yntema HG, Kroes T, Vulto-van Silfhout AT, Koolen DA, de Vries P, Gilissen C, del Rosario M, Hoischen A, Scheffer H, de Vries BBA, Brunner HG, Veltman JA, Vissers LELM. 2012. Diagnostic exome sequencing in persons with severe intellectual disability. *N Engl J Med* **367**:1921–1929.

Dräger UC. 1981. Observations on the organization of the visual cortex in the reeler mouse. *J Comp Neurol* **201**:555–570.

Duan X, Krishnaswamy A, De la Huerta I, Sanes JR. 2014. Type II cadherins guide assembly of a direction-selective retinal circuit. *Cell* **158**:793–807.

Duan X, Krishnaswamy A, Laboulaye MA, Liu J, Peng Y-R, Yamagata M, Toma K, Sanes JR. 2018. Cadherin combinations recruit dendrites of distinct retinal neurons to a shared interneuronal scaffold. *Neuron* **99**:1145-1154.e6.

Erdmann B, Kirsch F-P, Rathjen FG, Moré MI. 2003. N-cadherin is essential for retinal lamination in the zebrafish. *Dev Dyn* **226**:570–577.

Fu X, Sun H, Klein WH, Mu X. 2006. Beta-catenin is essential for lamination but not neurogenesis in mouse retinal development. *Dev Biol* **299**:424–437.

Gil-Sanz C, Landeira B, Ramos C, Costa MR, Müller U. 2014. Proliferative defects and formation of a double cortex in mice lacking Mltt4 and Cdh2

in the dorsal telencephalon. *J Neurosci* **34**:10475–10487.
Gollisch T, Meister M. 2010. Eye smarter than scientists believed: neural computations in circuits of the retina. *Neuron* **65**:150–164.
Greenwald SH, Kuchenbecker JA, Roberson DK, Neitz M, Neitz J. 2014. S-opsin knockout mice with the endogenous M-opsin gene replaced by an L-opsin variant. *Vis Neurosci* **31**:25–37.
Guy J, Staiger JF. 2017. The functioning of a cortex without layers. *Front Neuroanat* **11**:54.
Guy J, Wagener RJ, Möck M, Staiger JF. 2015. Persistence of functional sensory maps in the absence of cortical layers in the somsatosensory cortex of reeler mice. *Cereb Cortex* **25**:2517–2528.
Harris TJC, Tepass U. 2010. Adherens junctions: from molecules to morphogenesis. *Nat Rev Mol Cell Biol* **11**:502–514.
Haverkamp S, Ghosh KK, Hirano AA, Wässle H. 2003. Immunocytochemical description of five bipolar cell types of the mouse retina. *J Comp Neurol* **455**:463–476.
Hori T, Fukutome M, Maejima C, Matsushima H, Kobayashi Kensuke, Kitazawa S, Kitahara R, Kitano K, Kobayashi Kenta, Moritoh S, Koike C. 2019. Gene delivery to cone photoreceptors by subretinal injection of rAAV2/6 in the mouse retina. *Biochem Biophys Res Commun* **515**:222–227.
Ikeda W, Nakanishi H, Miyoshi J, Mandai K, Ishizaki H, Tanaka M, Togawa A, Takahashi K, Nishioka H, Yoshida H, Mizoguchi A, Nishikawa S, Takai Y. 1999. Afadin: A key molecule essential for structural organization of cell-cell junctions of polarized epithelia during embryogenesis. *J Cell Biol* **146**:1117–1132.
Inagaki M, Irie K, Ishizaki H, Tanaka-Okamoto M, Morimoto K, Inoue E, Ohtsuka T, Miyoshi J, Takai Y. 2005. Roles of cell-adhesion molecules nectin 1 and nectin 3 in ciliary body development. *Development* **132**:1525–1537.
Johnson RE, Kerschensteiner D. 2014. Retrograde plasticity and differential competition of bipolar cell dendrites and axons in the developing retina. *Curr Biol* **24**:2301–2306.
Jones BW, Marc RE, Pfeiffer RL. 1995. Retinal degeneration, remodeling and plasticityWebvision: The Organization of the Retina and Visual System. Salt Lake City (UT): University of Utah Health Sciences Center.
Koike C, Nishida A, Akimoto K, Nakaya M-A, Noda T, Ohno S, Furukawa T. 2005. Function of atypical protein kinase C lambda in differentiating photoreceptors is required for proper lamination of mouse retina. *J Neurosci* **25**:10290–10298.
Kubo S, Yamamoto H, Kajimura N, Omori Y, Maeda Y, Chaya T, Furukawa T. 2021. Functional analysis of Samd11, a retinal photoreceptor PRC1 component, in establishing rod photoreceptor identity. *Sci Rep* **11**:4180.
Kuo SP, Yu W-Q, Srivastava P, Okawa H, Santina LD, Berson DM, Awatramani GB, Wong ROL, Rieke F. 2024. Cone bipolar cell synapses generate transient versus sustained signals in parallel ON pathways of the mouse retina. *bioRxiv*. doi:10.1101/2024.05.13.593825
Lee JY, Care RA, Kastner DB, Della Santina L, Dunn FA. 2022. Inhibition, but not excitation, recovers from partial cone loss with greater spatiotemporal

integration, synapse density, and frequency. *Cell Rep* **38**:110317.
Liu JS. 2011. Molecular genetics of neuronal migration disorders. *Curr Neurol Neurosci Rep* **11**:171–178.
Majima T, Ogita H, Yamada T, Amano H, Togashi H, Sakisaka T, Tanaka-Okamoto M, Ishizaki H, Miyoshi J, Takai Y. 2009. Involvement of afadin in the formation and remodeling of synapses in the hippocampus. *Biochem Biophys Res Commun* **385**:539–544.
Mangeol P, Massey-Harroche D, Sebbagh M, Richard F, Le Bivic A, Lenne P-F. 2024. The zonula adherens matura redefines the apical junction of intestinal epithelia. *Proc Natl Acad Sci U S A* **121**:e2316722121.
Masai I, Lele Z, Yamaguchi M, Komori A, Nakata A, Nishiwaki Y, Wada H, Tanaka H, Nojima Y, Hammerschmidt M, Wilson SW, Okamoto H. 2003. N-cadherin mediates retinal lamination, maintenance of forebrain compartments and patterning of retinal neurites. *Development* **130**:2479–2494.
Masland RH. 2012. The neuronal organization of the retina. *Neuron* **76**:266–280.
Meng W, Takeichi M. 2009. Adherens junction: molecular architecture and regulation. *Cold Spring Harb Perspect Biol* **1**:a002899.
Miao GG, Smeyne RJ, D'Arcangelo G, Copeland NG, Jenkins NA, Morgan JI, Curran T. 1994. Isolation of an allele of reeler by insertional mutagenesis. *Proc Natl Acad Sci U S A* **91**:11050–11054.
Nahar A, Cho S-H. 2022. Current perspectives in Leber congenital amaurosis type 8 mouse modeling. *Dev Dyn* **251**:1094–1106.
Nikolaou N, Meyer MP. 2015. Lamination speeds the functional development of visual circuits. *Neuron* **88**:999–1013.
Ohama D, Matsuda T, Oinuma I. 2018. Differential regional and subcellular localization patterns of afadin splice variants in the mouse central nervous system. *Brain Res* **1692**:74–86.
Okawa H, Della Santina L, Schwartz GW, Rieke F, Wong ROL. 2014. Interplay of cell-autonomous and nonautonomous mechanisms tailors synaptic connectivity of converging axons in vivo. *Neuron* **82**:125–137.
Pan Y-H, Wu N, Yuan X-B. 2019. Toward a better understanding of neuronal migration deficits in autism spectrum disorders. *Front Cell Dev Biol* **7**:205.
Park C, Falls W, Finger JH, Longo-Guess CM, Ackerman SL. 2002. Deletion in Catna2, encoding alpha N-catenin, causes cerebellar and hippocampal lamination defects and impaired startle modulation. *Nat Genet* **31**:279–284.
Poria D, Dhingra NK. 2015. Spontaneous oscillatory activity in rd1 mouse retina is transferred from ON pathway to OFF pathway via glycinergic synapse. *J Neurophysiol* **113**:420–425.
Puthussery T, Gayet-Primo J, Taylor WR. 2010. Localization of the calcium-binding protein secretagogin in cone bipolar cells of the mammalian retina. *J Comp Neurol* **518**:513–525.
Quiroga RQ, Nadasdy Z, Ben-Shaul Y. 2004. Unsupervised spike detection and sorting with wavelets and superparamagnetic clustering. *Neural Comput* **16**:1661–1687.
Romero DM, Bahi-Buisson N, Francis F. 2018. Genetics and mechanisms

leading to human cortical malformations. *Semin Cell Dev Biol* **76**:33–75.
Sakakibara S, Maruo T, Miyata M, Mizutani K, Takai Y. 2018. Requirement of the F-actin-binding activity of l-afadin for enhancing the formation of adherens and tight junctions. *Genes Cells* **23**:185–199.
Sato S, Inoue T, Terada K, Matsuo I, Aizawa S, Tano Y, Fujikado T, Furukawa T. 2007. Dkk3-Cre BAC transgenic mouse line: a tool for highly efficient gene deletion in retinal progenitor cells. *Genesis* **45**:502–507.
Sato T, Fujita N, Yamada A, Ooshio T, Okamoto R, Irie K, Takai Y. 2006. Regulation of the assembly and adhesion activity of E-cadherin by nectin and afadin for the formation of adherens junctions in Madin-Darby canine kidney cells. *J Biol Chem* **281**:5288–5299.
Sebbagh M, Schwartz MA. 2024. Afadin-nectin forces its way to the front. *J Cell Biol* **223**. doi:10.1083/jcb.202403177
Shen N, Wang B, Soto F, Kerschensteiner D. 2020. Homeostatic plasticity shapes the retinal response to photoreceptor degeneration. *Curr Biol* **30**:1916-1926.e3.
Solovei I, Kreysing M, Lanctôt C, Kösem S, Peichl L, Cremer T, Guck J, Joffe B. 2009. Nuclear architecture of rod photoreceptor cells adapts to vision in mammalian evolution. *Cell* **137**:356–368.
Stouffer MA, Golden JA, Francis F. 2016. Neuronal migration disorders: Focus on the cytoskeleton and epilepsy. *Neurobiol Dis* **92**:18–45.
Strettoi E, Di Marco B, Orsini N, Napoli D. 2022. Retinal plasticity. *Int J Mol Sci* **23**:1138.
Stuck MW, Conley SM, Naash MI. 2012. Defects in the outer limiting membrane are associated with rosette development in the Nrl-/- retina. *PLoS One* **7**:e32484.
Tachibana K, Nakanishi H, Mandai K, Ozaki K, Ikeda W, Yamamoto Y, Nagafuchi A, Tsukita S, Takai Y. 2000. Two cell adhesion molecules, nectin and cadherin, interact through their cytoplasmic domain-associated proteins. *J Cell Biol* **150**:1161–1176.
Takai Y, Ikeda W, Ogita H, Rikitake Y. 2008a. The immunoglobulin-like cell adhesion molecule nectin and its associated protein afadin. *Annu Rev Cell Dev Biol* **24**:309–342.
Takai Y, Miyoshi J, Ikeda W, Ogita H. 2008b. Nectins and nectin-like molecules: roles in contact inhibition of cell movement and proliferation. *Nat Rev Mol Cell Biol* **9**:603–615.
Takai Y, Nakanishi H. 2003. Nectin and afadin: novel organizers of intercellular junctions. *J Cell Sci* **116**:17–27.
Takeuchi H, Horie S, Moritoh S, Matsushima H, Hori T, Kimori Y, Kitano K, Tsubo Y, Tachibana M, Koike C. 2018. Different activity patterns in retinal ganglion cells of TRPM1 and mGluR6 knockout mice. *Biomed Res Int* **2018**:2963232.
Tanimoto N, Sothilingam V, Kondo M, Biel M, Humphries P, Seeliger MW. 2015. Electroretinographic assessment of rod- and cone-mediated bipolar cell pathways using flicker stimuli in mice. *Sci Rep* **5**:10731.
The electroretinogram: ERG by Ido Perlman. n.d. https://webvision.med.utah.edu/book/electrophysiology/the-electroretinog

ram-erg/
Ueno A, Omori Y, Sugita Y, Watanabe S, Chaya T, Kozuka T, Kon T, Yoshida S, Matsushita K, Kuwahara R, Kajimura N, Okada Y, Furukawa T. 2018. Lrit1, a retinal transmembrane protein, regulates selective synapse formation in cone photoreceptor cells and visual acuity. *Cell Rep* **22**:3548–3561.
Veeraval L, O'Leary CJ, Cooper HM. 2020. Adherens junctions: Guardians of cortical development. *Front Cell Dev Biol* **8**:6.
Wässle H. 2004. Parallel processing in the mammalian retina. *Nat Rev Neurosci* **5**:747–757.
Willbold E, Layer PG. 1998. Müller glia cells and their possible roles during retina differentiation in vivo and in vitro. *Histol Histopathol* **13**:531–552.
Xu H, Enemchukwu N, Zhong X, Zhang O, Fu Y. 2020. Deletion of M-opsin prevents M cone degeneration in a mouse model of Leber congenital amaurosis. *Am J Pathol* **190**:1059–1067.
Yamamoto H, Kon T, Omori Y, Furukawa T. 2020. Functional and evolutionary diversification of Otx2 and Crx in vertebrate retinal photoreceptor and bipolar cell development. *Cell Rep* **30**:658-671.e5.
Yamasaki S, Tu H-Y, Matsuyama T, Horiuchi M, Hashiguchi T, Sho J, Kuwahara A, Kishino A, Kimura T, Takahashi M, Mandai M. 2022. A Genetic modification that reduces ON-bipolar cells in hESC-derived retinas enhances functional integration after transplantation. *iScience* **25**:103657.
Zapp SJ, Nitsche S, Gollisch T. 2022. Retinal receptive-field substructure: scaffolding for coding and computation. *Trends Neurosci* **45**:430–445.
Zhang P-M, Wu J-Y, Zhou Y, Liang P-J, Yuan J-Q. 2004. Spike sorting based on automatic template reconstruction with a partial solution to the overlapping problem. *J Neurosci Methods* **135**:55–65.

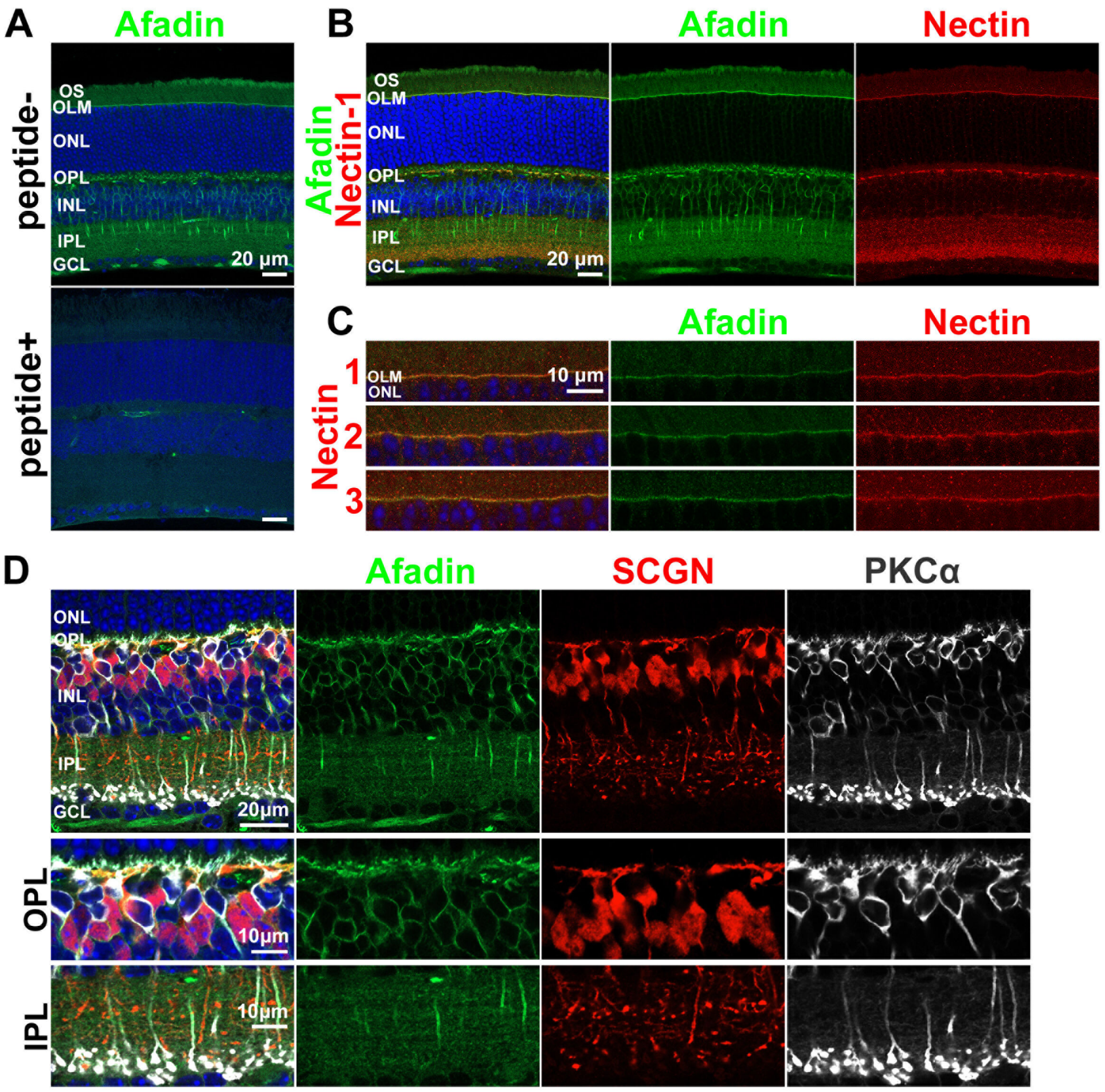
A
Afadin
peptide-
peptide+
OS
OLM
ONL
OPL
INL
IPL
GCL
20 µm
B
Afadin
Nectin
Afadin
Nectin-1
OS
OLM
ONL
OPL
INL
IPL
GCL
20 µm
C
Afadin
Nectin
Nectin
1
2
3
OLM
ONL
10 µm
D
Afadin
SCGN
PKCα
ONL
OPL
INL
IPL
GCL
20µm
OPL
10µm
IPL
10µm

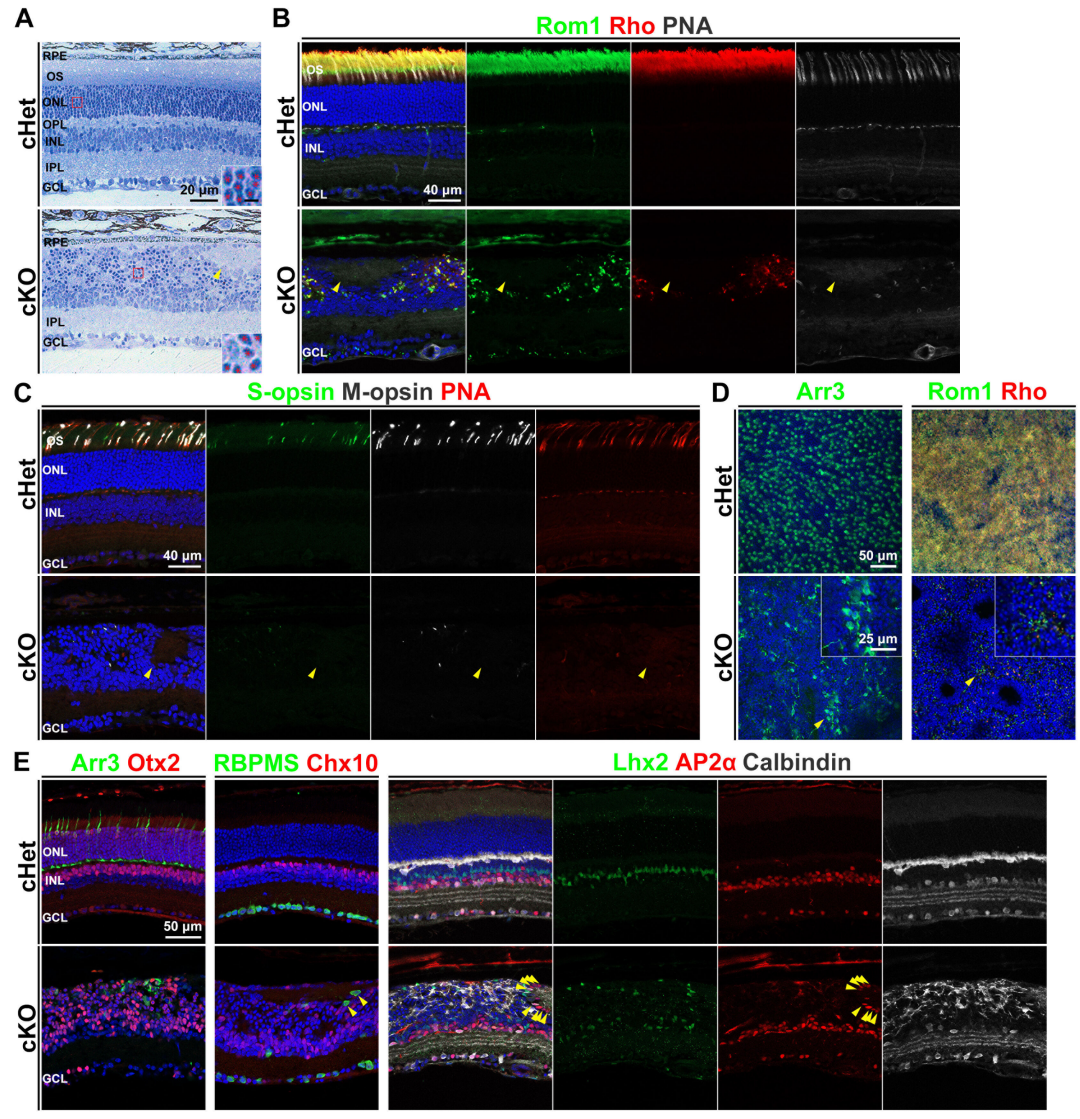
A
cHet
RPE
OS
ONL
OPL
INL
IPL
GCL
20 μm
cKO
RPE
IPL
GCL
B
Rom1 Rho PNA
cHet
OS
ONL
INL
GCL
40 μm
cKO
GCL
C
S-opsin M-opsin PNA
cHet
OS
ONL
INL
GCL
40 μm
cKO
GCL
D
Arr3
Rom1 Rho
cHet
50 μm
cKO
25 μm
E
Arr3 Otx2
RBPMS Chx10
Lhx2 AP2α Calbindin
cHet
ONL
INL
GCL
50 μm
cKO
GCL

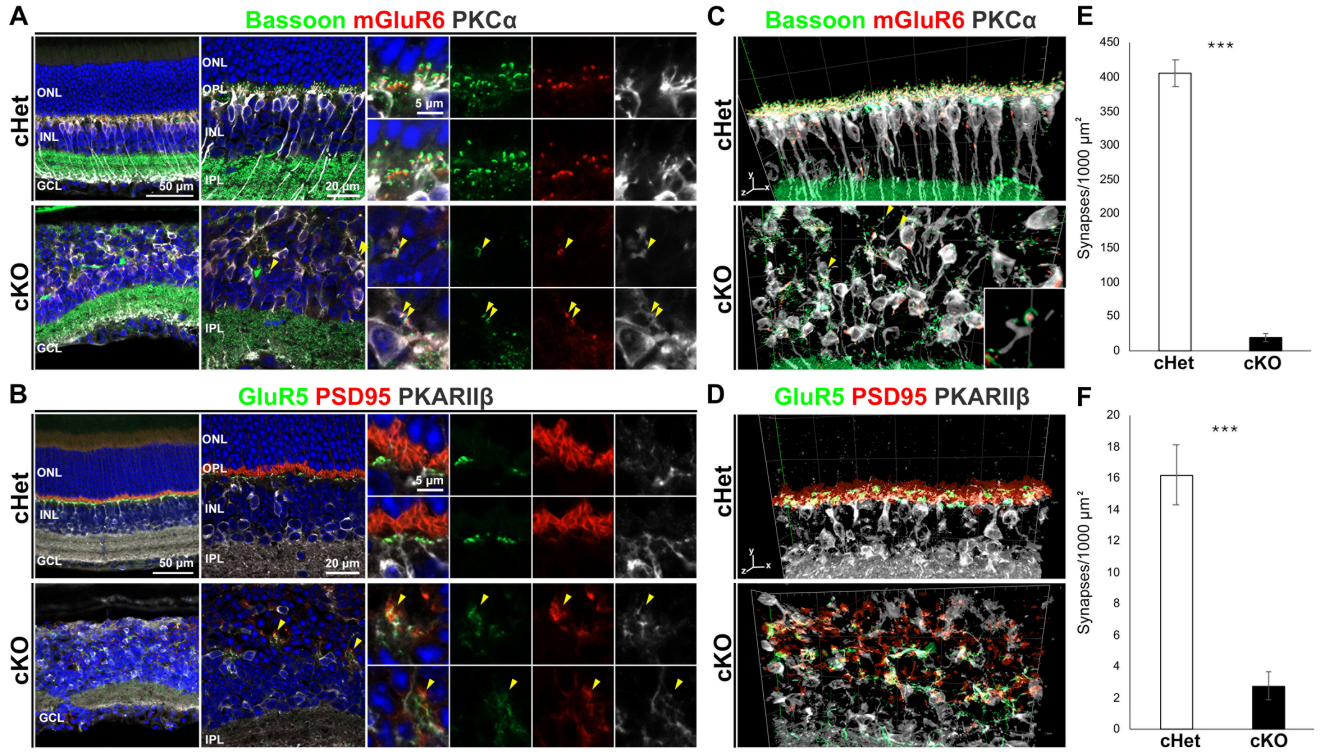
A
Bassoon mGluR6 PKCα
cHet
cKO
ONL
OPL
INL
IPL
GCL
50 µm
20 µm
5 µm
B
GluR5 PSD95 PKARIIβ
C
D
E
F
Synapses/1000 µm²
***
cHet
cKO

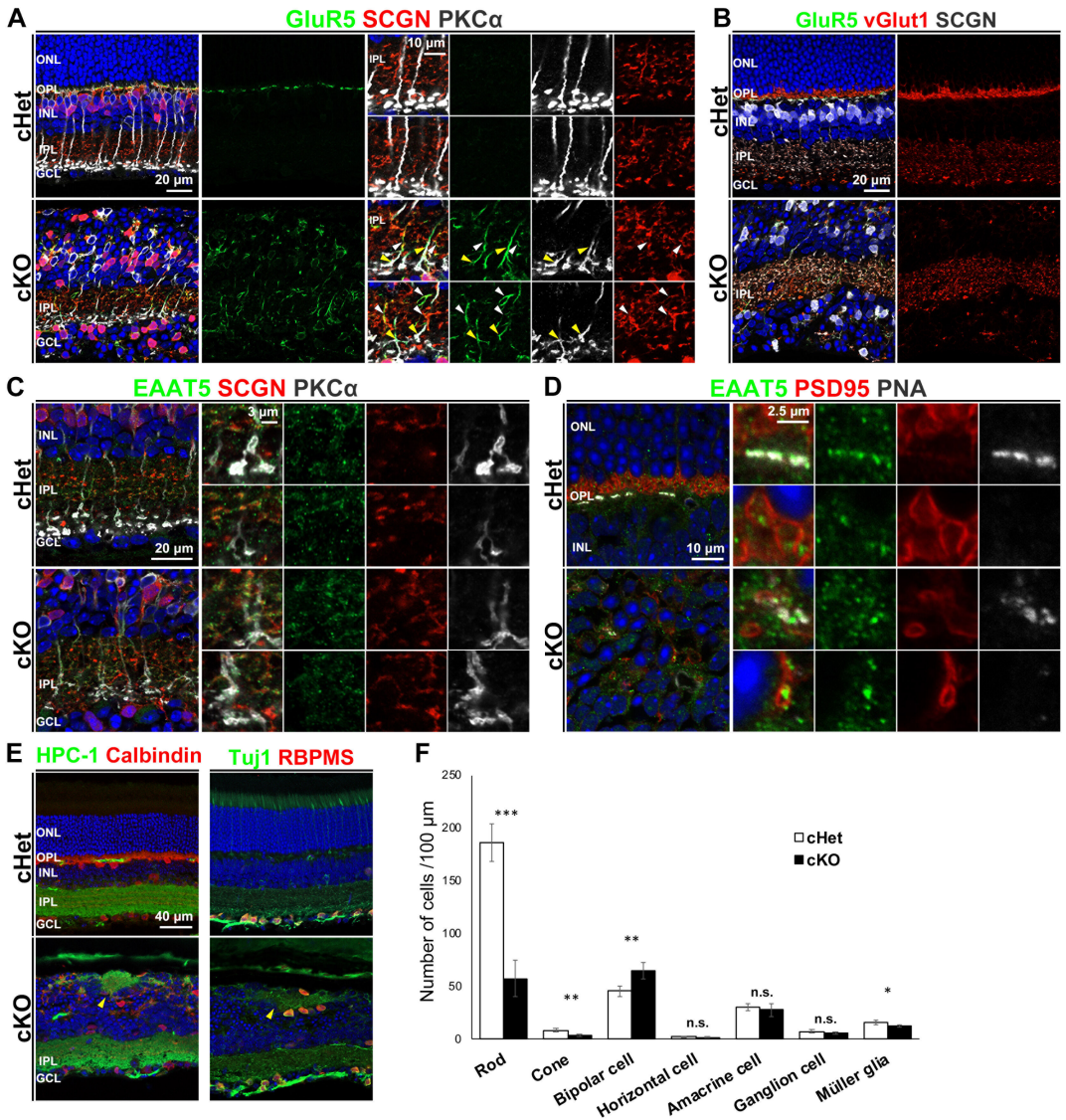
A
GluR5 SCGN PKCα
cHet
cKO
ONL
OPL
INL
IPL
GCL
20 μm
10 μm
B
GluR5 vGlut1 SCGN
C
EAAT5 SCGN PKCα
3 μm
D
EAAT5 PSD95 PNA
2.5 μm
E
HPC-1 Calbindin
Tuj1 RBPMS
40 μm
F
Number of cells /100 μm
cHet
cKO
Rod
Cone
Bipolar cell
Horizontal cell
Amacrine cell
Ganglion cell
Müller glia
n.s.

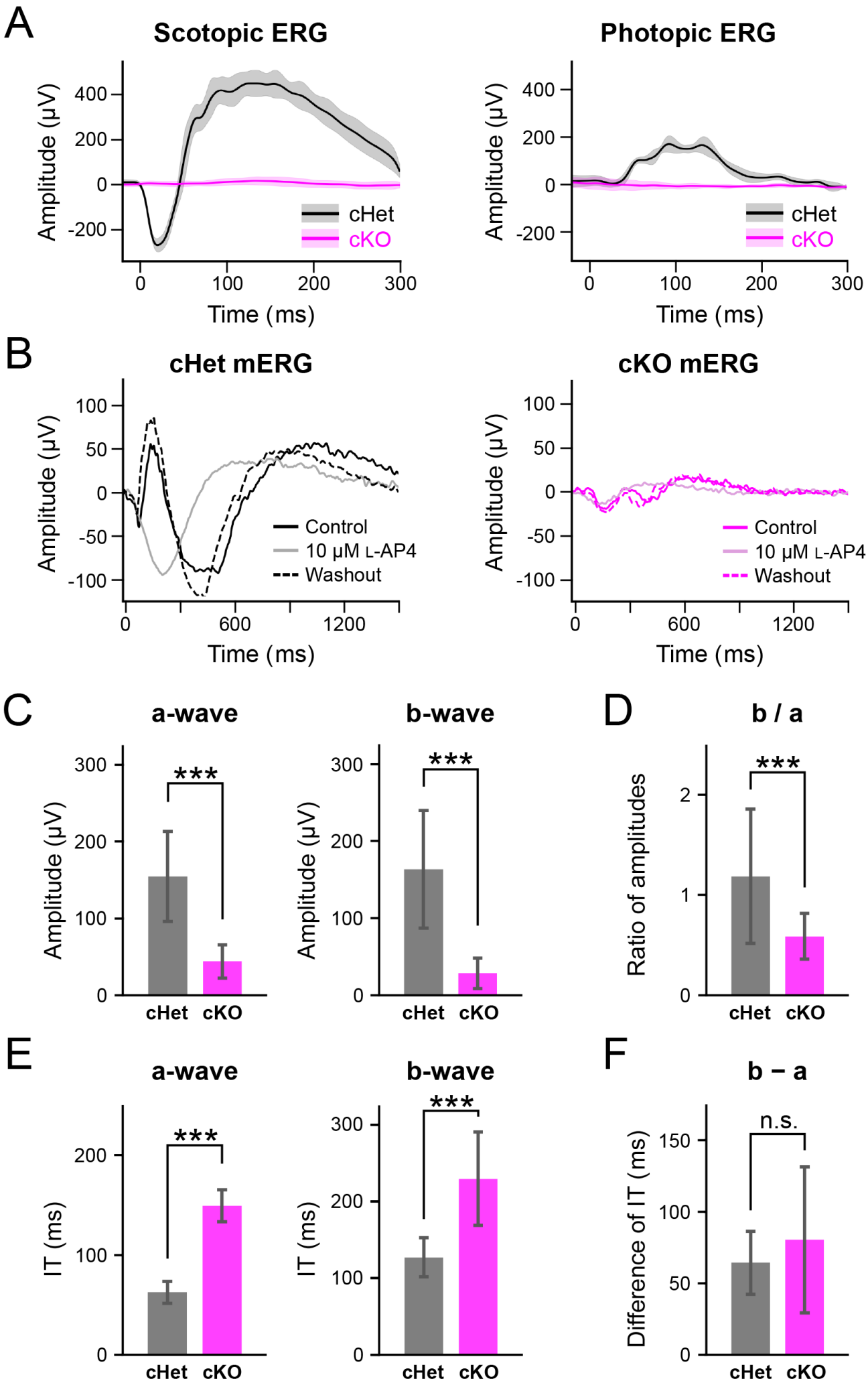
A
Scotopic ERG
Photopic ERG
Amplitude (μV)
400
200
0
-200
0
100
200
300
Time (ms)
cHet
cKO
B
cHet mERG
cKO mERG
100
50
0
-50
-100
0
600
1200
Control
10 μM L-AP4
Washout
C
a-wave
b-wave
D
b / a
***
Amplitude (μV)
Ratio of amplitudes
cHet
cKO
E
a-wave
b-wave
F
b − a
IT (ms)
Difference of IT (ms)
n.s.

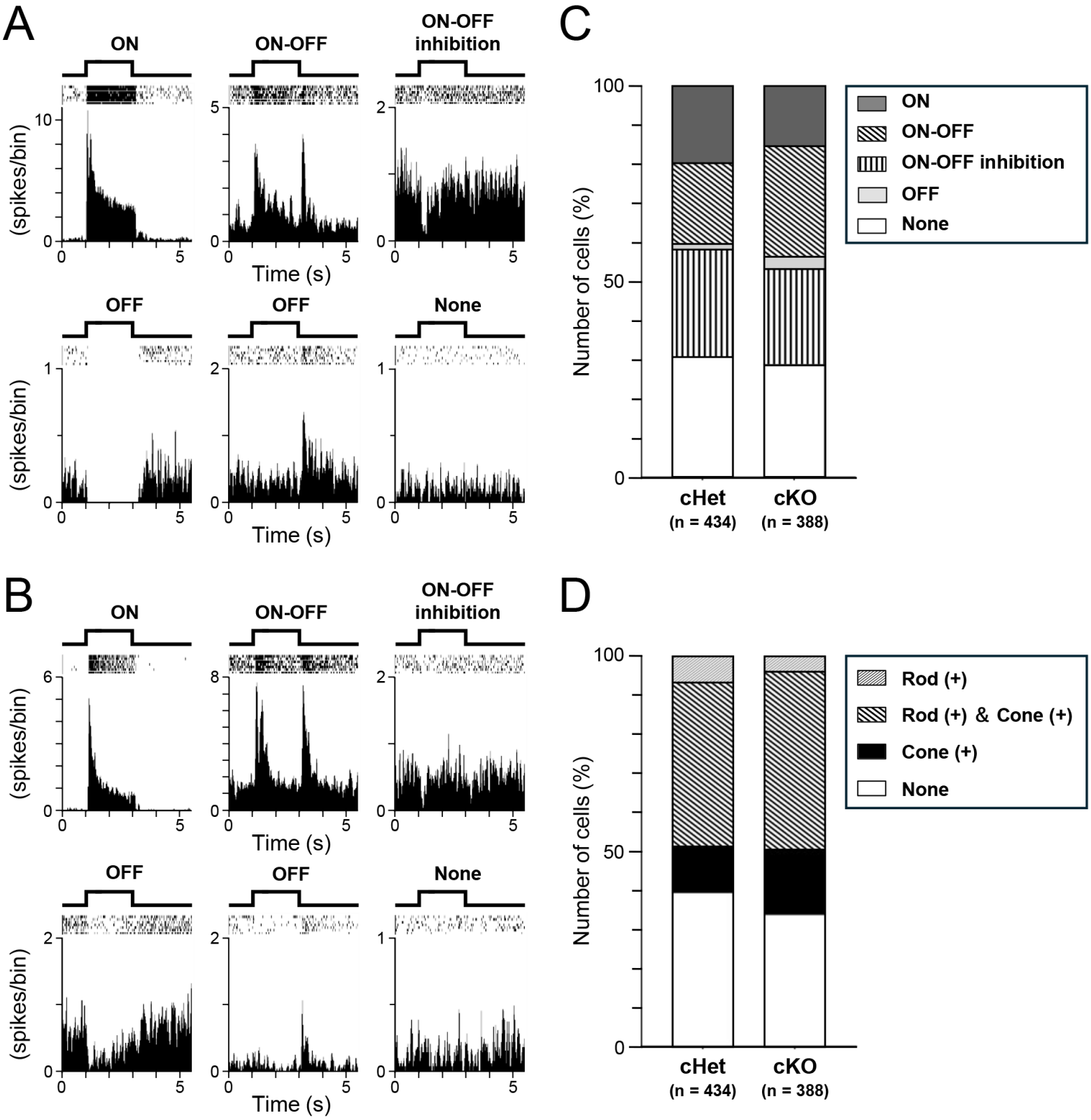
A
ON
ON-OFF
ON-OFF inhibition
OFF
OFF
None
(spikes/bin)
Time (s)
B
ON
ON-OFF
ON-OFF inhibition
OFF
OFF
None
(spikes/bin)
Time (s)
C
Number of cells (%)
ON
ON-OFF
ON-OFF inhibition
OFF
None
cHet
(n = 434)
cKO
(n = 388)
D
Number of cells (%)
Rod (+)
Rod (+) & Cone (+)
Cone (+)
None
cHet
(n = 434)
cKO
(n = 388)

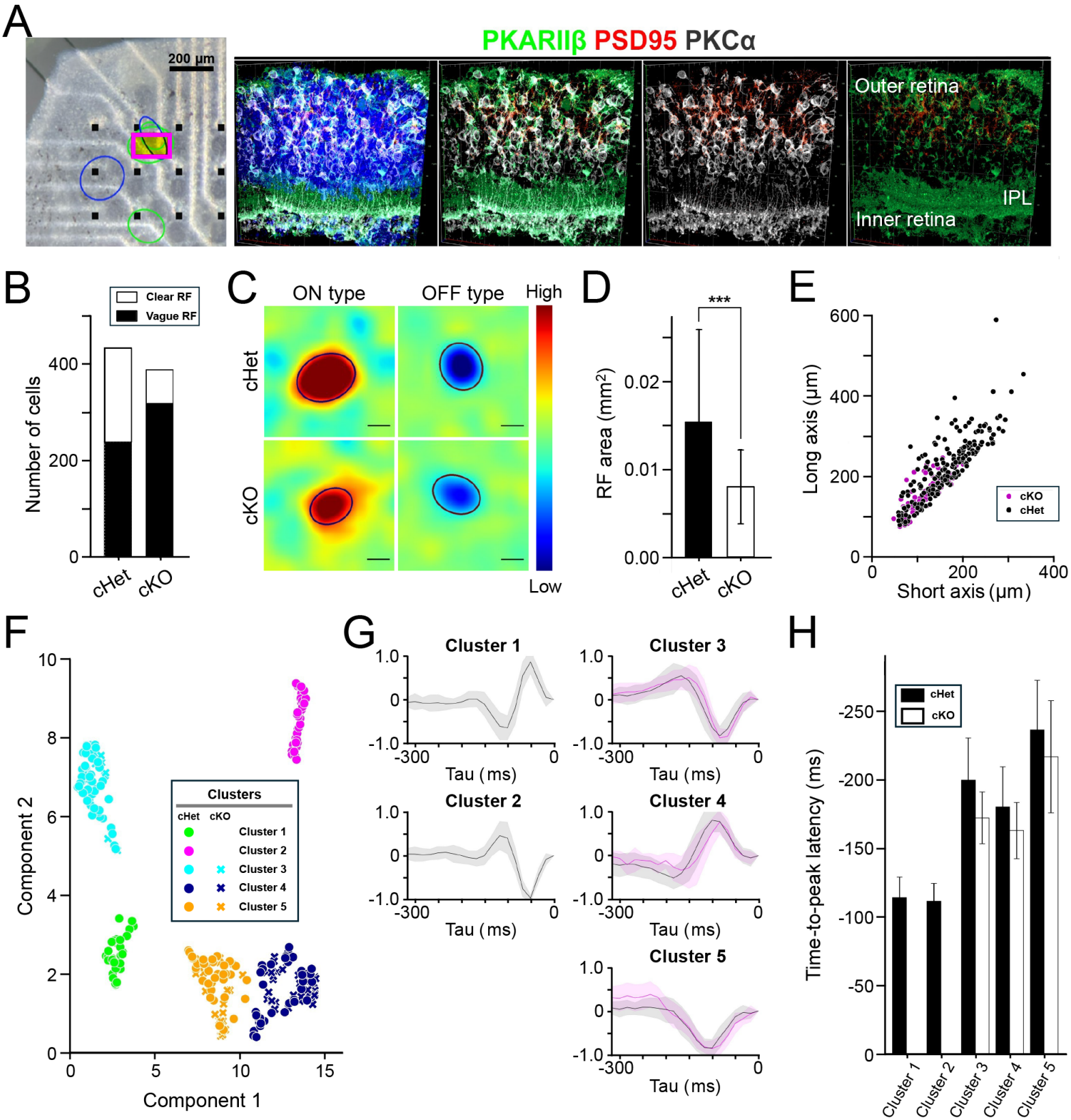
A
200 µm
PKARIIβ PSD95 PKCα
Outer retina
IPL
Inner retina
B
Clear RF
Vague RF
Number of cells
400
200
0
cHet
cKO
C
ON type
OFF type
High
Low
cHet
cKO
D
***
RF area (mm²)
0.02
0.01
0.00
cHet
cKO
E
Long axis (µm)
600
400
200
0
Short axis (µm)
cKO
cHet
F
Component 2
Component 1
Clusters
cHet cKO
Cluster 1
Cluster 2
Cluster 3
Cluster 4
Cluster 5
G
Cluster 1
Cluster 2
Cluster 3
Cluster 4
Cluster 5
Tau (ms)
H
Time-to-peak latency (ms)
cHet
cKO
Cluster 1
Cluster 2
Cluster 3
Cluster 4
Cluster 5

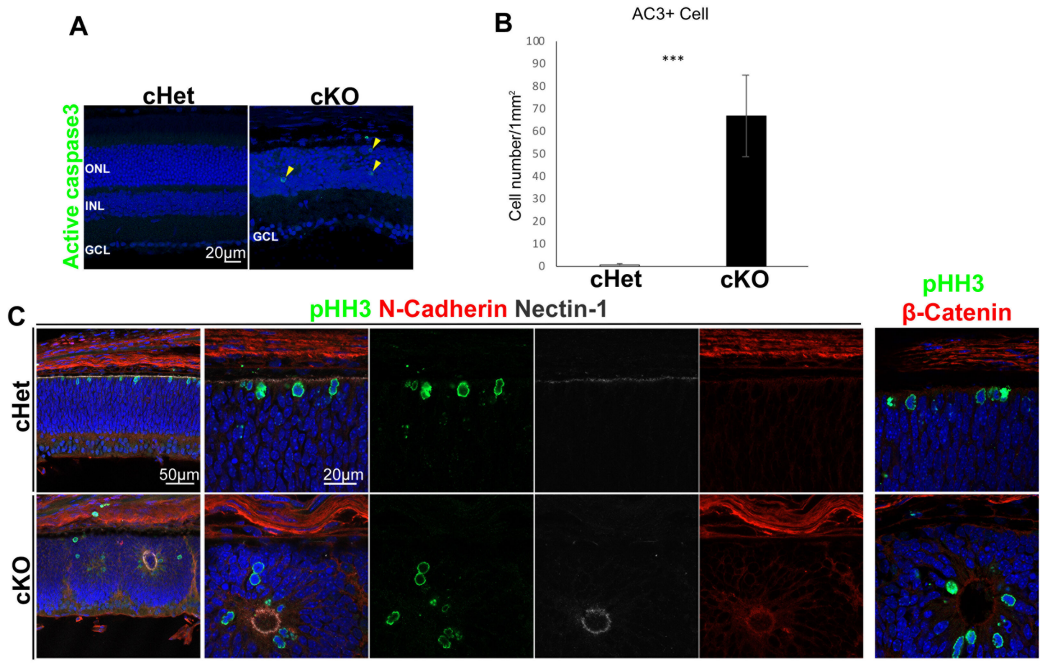
A
cHet
cKO
Active caspase3
ONL
INL
GCL
20μm
GCL
B
AC3+ Cell
***
Cell number/1mm²
100
90
80
70
60
50
40
30
20
10
0
cHet
cKO
C
pHH3 N-Cadherin Nectin-1
cHet
cKO
50μm
20μm
pHH3
β-Catenin